Response and Failure of Adhesively Bonded Automotive Composite Structures under Impact Loads

Joshua C. Simón

Thesis submitted to the Faculty of the Virginia Polytechnic

Institute and State University in partial fulfillment

of the requirements for the degree of

Master of Science

in

Mechanical Engineering

David A. Dillard, Chair

Robert West

Eric Johnson

August 6, 2004

Blacksburg, Virginia

Keywords: Fracture, Impact, Mode I, Mode II, Mixed-Mode I/II, Adhesive Joint, Composite, Unstable Growth, Stick-Slip

Response and Failure of Adhesively Bonded Automotive Composite Structures under Impact Loads

Joshua C. Simón

Abstract

An experimental technique for conducting low speed impact of adhesively bonded automotive composite joints is presented. Based on the use of a modified drop tower, mode I, II, and mixed mode values for critical energy release rate were determined for a composite/epoxy system and used to create a fracture failure envelope. Because load measurements become erratic and unreliable at higher test rates, displacement-based relationships were used to quantify these energy release rates. Displacement data was collected with an imaging system that utilized edge detection to determine displacement profiles, end displacements, and opening displacements where applicable. Because of the resolution of the image-based approach used, determining crack length experimentally was extremely difficult. As a result, numerical methods were developed to objectively determine the crack length based on the available experimental data in mode I, II, and mixed mode I/II configurations.

This numerical method uses a nonlinear fit to determine mode I crack lengths and a theoretical model based on cubic equations for mode II and mixed-mode I/II, where the coefficients of the equations are determined by using both boundary and transition conditions that are a result of the test setup. A double cantilever beam (DCB) geometry was chosen to collect mode I data, an end-loaded split (ELS) geometry was used for mode II, and a single leg bend (SLB) geometry was used for mixed-mode I/II. These geometries were used to determine the fracture characteristics of adhesively bonded

automotive composites to create fracture failure envelopes as well as provide mode I, II, and mixed-mode I/II data to be used in finite element models.

The chosen adhesive exhibited unstable, stick-slip crack growth, which resulted in very few data points being collected from each static DCB specimen as well as drastic drops in energy release rate between initiation and arrest points. Unstable growth also created issues in dynamic testing, as data points surrounding these "stick-slip" events were lost due to the insufficient sampling rate of the available imaging system.

Issues also arose with differences between thick and thin composite adherend specimens. These differences could result from additional curing in thick adherend composite specimens due to the adherends retaining heat. DSC testing was conducted on uncured adhesive using a 2, 5, and 10 minute hold at the cure temperature, and significant additional curing was observed between the two and five minute cures. Due to the difference in relative stiffness between the 12 and 36 ply composite, the local loading rate at the crack tip was lower in the 12 ply adherends, possibly allowing for a larger plastic zone and thus a higher energy release rate. As a result, tests were conducted on 36 ply composite specimens at rates of 1 mm/min and 0.1 mm/min to determine if there were loading rate effects. This testing showed that higher initiation energy relase rates were found at the lower test rate, thus reinforcing the local loading rate theory.

Due to issues with plastic deformation in aluminum adherends, mode II and mixed-mode I/II data were collected using only composite adherends. Only one data point was collected per specimen as the crack propagated directly into the composite after initiating from the precrack, thus multiple tests were conducted to collect sufficient data for constructing a failure envelope.

Once mode I, II and mixed-mode I/II fracture data was collected, a fracture failure envelope was created. This failure envelope, combined with a predetermined factor of safety, could provide some of the necessary tools for design with this adhesive/composite system.

Acknowledgements

I would like to thank the project monitor Dr. Naveen Rastogi for technical discussions held with him. I also acknowledge that this research is supported, in whole or in part, by the Department of Energy cooperative agreement number DE-FC05-95OR22363. Such support does not constitute an endorsement by the Department of Energy of the views expressed herein. Furthermore, I would also like to acknowledge the interdisciplinary research environment fostered by the Center for Adhesive and Sealant Science and the Engineering Science and Mechanics Department at Virginia Tech for the use of their facilities and equipment. Thanks also to the following people who helped greatly with this research: Steve Brown, Jeremy Garrett, Mike Christopher, Josh Grohs, John Hennage, Jordan Haines, and last but certainly not least, my wife Kimberly Simón.

Contents

List of Figures

List of Tables

Chapter 1: Introduction

1.1: Background

The use of adhesives in place of traditional fasteners is becoming increasingly popular in structural design. Structural adhesive technology was pioneered in the aircraft industry, but has been transferred to everything from automobiles to buildings. Adhesives are materials of choice for many applications because they enable lightweight designs, can be used to join dissimilar materials, and are often cheaper than traditional fasteners to use and apply. They also provide a greater contact area than that of a bolted joint and thus a more efficient stress distribution[1].

There have been many material advancements in recent years that lend themselves to the use of adhesives. Advanced composite materials have become crucial in the design of aircraft, and are becoming increasingly popular for use in automobiles and even civil infrastructure. Many of these brittle materials cannot be assembled with bolts and other traditional fasteners due to wear and corrosion from combining dissimilar materials as well as stress concentration factors, thus requiring other methods of attachment. Traditional methods of attachment for automotive body panels such as spot welds are also not appropriate for composite or hybrid (aluminum to steel etc.) joints, leading to increased use of structural adhesives in current and anticipated automotive bodies. These factors have led to the extensive use of adhesives in modern design. Structural adhesives, or adhesives used in load-bearing structures, are the focus of this research. These adhesives are generally thermosetting (although thermoplastics have made recent inroads), and are characterized by a high modulus of elasticity and strength[2].

The field of structural design is based heavily on failure criteria to determine appropriate design envelopes. The most common is the strength approach, which is used

for designing with metals, concrete, and some polymers. Examples of this type of approach are the maximum shear stress and distortional energy theories[3]. A fracture based approach is also used in many areas of design, from piping to nuclear reactors as well as adhesives, as many failures in bonded joints are due to crack growth within the adhesive layer.

The fracture-based approach derives from continuum fracture mechanics theory, which claims the strength of most real solids is governed by flaws within the material[2]. To help predict this type of behavior, many test methods have been developed to determine fracture properties of adhesives. These tests are used to characterize the mode I, II, and III fracture properties of many types of material systems. In this study, the focus will be on the mode I and II characteristics of bonded composite joints for automotive applications.

1.2: Goals and Significance

The goal of this research was to study the fracture properties of adhesively bonded composite structures in mode I, II, and mixed-mode I/II loading to create fracture failure envelopes for these modes to be used in design. The main emphasis was dynamic loading of these structures, but quasi-static testing was also conducted to provide a means of comparison for dynamic data. Aluminum adherends were also used as a baseline for comparison in some cases.

The prescribed loading modes were accomplished using double cantilever beam (mode I), end-loaded split (mode II), and single leg bend (mixed-mode I/II) geometries. An Instron (Canton, MA) 4500 series test frame was used for quasi-static loading, and a Dynatup (Canton, MA) drop tower and Kodak (San Diego, CA) Ekta Pro high-speed

video camera were used to collect dynamic data. Adhesive cure properties were also collected using a TA Instruments DSC2920 differential scanning calorimeter (New Castle, DE).

1.3: Thesis Organization

This report will begin with a review of relevant literature to give background and support to the methods and ideas used in this testing. Following the literature review, materials, specimen preparation, and test methods/equipment will be discussed. Finally analysis methods, test results, and conclusions will be presented. The chapter layout is as follows:

Chapter 1 gives a brief introduction to the topic of this research as well as background information on the use of adhesives in modern design.

Chapter 2 reviews literature relevant to the topics of this research including: test method standardization, general fracture mechanics, test methods for modes I, II, and mixed-mode I/II fracture testing, behavior and properties of brittle adhesives, and data analysis methods for fracture testing.

Chapter 3 focuses on the test methods employed to gather the data presented in this thesis, including static and dynamic double cantilever beam, end-loaded split, and single leg bend tests.

Chapter 4 covers the data analysis methods utilized to reduce test data collected using the methods described in Chapter 3.

Chapter 5 presents the results of this testing as well as relevant insight into trends and phenomena found during the testing and analysis process.

Chapter 6 includes a summary of the project as well as relevant conclusions.

Finally, Appendix A discusses the use of the Hutchinson and Suo method to determine possible mode mixities with the provided adherend thicknesses, Appendix B presents the crack blunting model developed by Kinloch and Williams, Appendix C outlines the P2 etching process performed on aluminum adherends, and Appendix D presents the analysis code developed to analyze mode II and mixed-mode data[4,5].

References

1. Rakestraw, M.D., Taylor, M.W., Dillard, D.A., "Time dependent crack growth and loading rate effects on interfacial and cohesive fracture of adhesive joints," *Journal of Adhesion*, **55** (1995), 123-149.
2. Gledhill, R.A., Kinloch, A.J., "Mechanics of crack growth in epoxide resins," *Polymer Engineering and Science*, **19** (1979), 82-88.
3. Shigley, J.E., Mischke, C.R. *Mechanical Engineering Design*. New York: McGraw-Hill, 2001.
4. Hutchinson, J.W., Suo, Z., "Mixed mode cracking in layered materials," *Advance in Applied Mechanics*, **29** (1992), 63-189.
5. Kinloch, A.J., Williams, J.G., "Crack blunting mechanisms in polymers," *Journal of Materials Science*, **15** (1980), 987-996.

Chapter 2: Literature Review

2.1: Introduction

The growing need for fracture characterization in structural adhesive applications has led to the development of test methods to evaluate new material systems in a variety of loading conditions. Some of these conditions include pure opening, or mode I, pure forward shear, or mode II, and mixed-mode I/II, a combination of opening and shear loading. There have been many tests developed for these geometries by various researchers, but few have been standardized by the American Society for Testing and Materials (ASTM)[1]. For mode I characterization, the double cantilever beam (DCB) geometry is the accepted standard, and is shown schematically in Figure 2.1.

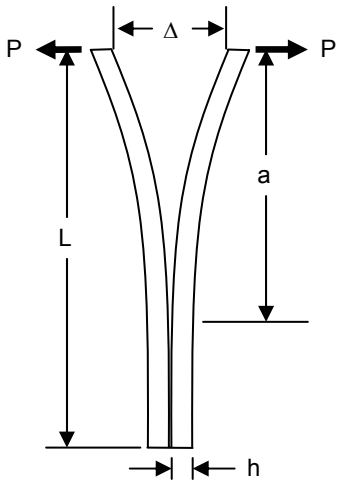

Figure 2.1. A schematic diagram of the double cantilever beam geometry

The DCB geometry is used for determining the Mode I energy release rate and will be discussed in further detail in a later chapter. A mixed mode bending test to determine properties for a variety of mode I and mode II has also been developed into an ASTM standard, but will not be discussed as it was not used in this research[2].

2.1.1: Standardization

In a recent publication, O'Brien has discussed the process of test method standardization and how it applies to fracture testing[1]. As previously discussed, the double cantilever beam geometry has been accepted as an ASTM standard, and at the time of O'Brien's writing, was under review by the International Organization for Standardization (ISO)[1]. The mixed-mode bending geometry has also been standardized by ASTM, but was not up for review by ISO at that time.

The most common mode II tests are the end-notched flexure (ENF) test and the end-loaded split (ELS) test. Although frequently used, neither one of these geometries was standardized as of O'Brien's writing[1]. The ENF geometry, shown in Figure 2.2, is centrally loaded with the uncracked end of the specimen fixed, while the cracked end is placed on a roller to help induce a pure shear load[1]. The ELS geometry, shown in Figure 2.3, is a cantilever setup that is loaded at the free end, where the precrack is located, and is fixed at the uncracked end to provide a zero slope condition[1]. Both of these methods provide the same fracture mode, thus the geometry selection is dictated in most cases by available equipment.

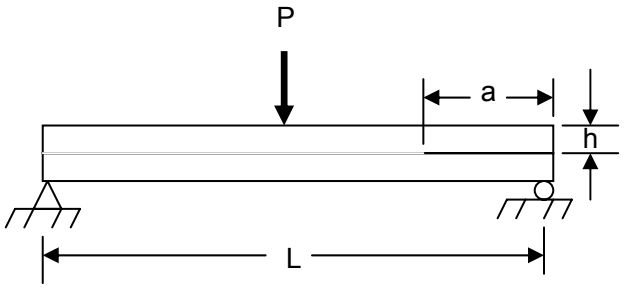

Figure 2.2. A schematic diagram of the end-notched flexure geometry

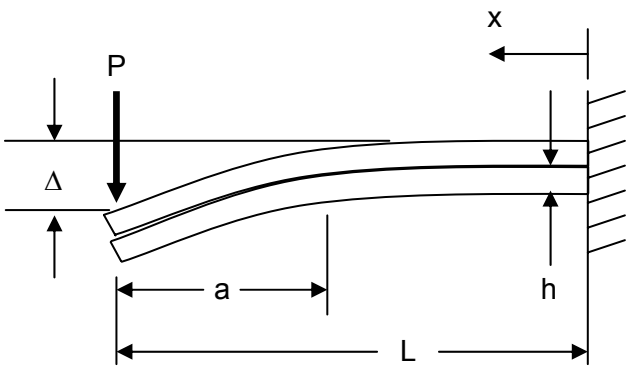

Figure 2.3. A schematic diagram of the end-loaded split geometry

The process to standardization for any test method is long, consisting of many steps, especially in dealing with international standardization. With time, more test methods to characterize fracture will be standardized and adopted into international practice. As in the past, emerging technologies will drive the standardization process forward to create robust methods to determine fracture based design parameters.

2.1.2: Test Comparisons

With many test geometries available for fracture testing, a means to compare them is helpful so that a suitable test can be chosen for a given situation. Many different approaches to this problem have been presented, but here only two, most relevant to this research, will be discussed.

The first comparison method to be discussed is the fracture efficiency parameter developed by Lai and Dillard to relate the energy release rate to the square of the maximum non-singular stress, thus relating the likelihood of debonding to adherend yield, damage, or failure[3]. This method was developed to provide a comparison between the multitudes of tests used on coatings and laminated beams. In this thesis, the focus will be on the laminated beam fracture efficiency parameters, since this topic is most

relevant to the testing of adhesively bonded joints. The fracture efficiency is very useful for choosing test geometries, as it provides a straightforward way to estimate whether a certain geometry will cause yielding or rupturing within the adherend material before fracture conditions are satisfied and a crack can propagate within the adhesive layer. This is crucial in research that is constrained by time, as it helps to reduce unforeseen issues in test design.

The efficiency parameter is derived from an energy release rate (or fracture energy) term expressed in terms of a maximum stress. This equation is then modified to give the fracture efficiency parameter, which indicates the ability of a geometry to produce a maximum energy release rate at a given maximum non-singular stress level[3]:

$$T_e = \frac{G}{\sigma_{\max}^2} \tag{1}$$

where G is the energy release rate, and σ_{max} is the maximum non-singular stress level. This parameter can then be normalized by dividing by the critical fracture efficiency parameter:

$$T_e^c = \frac{\Gamma}{\sigma_{cr}^2} \tag{2}$$

where Γ is the critical debond energy and σ_{cr} is the adherend critical stress of the material system being studied. To prevent yielding or fracture within the adherends for a given geometry, this parameter must be greater than unity. Thus, by taking known test parameters, one can determine whether a test will produce the desired results.

Another useful piece of information for fracture testing is the phase angle. This angle is useful in determining the relative mode mixity of a specific geometry and also in combining a set of tests to provide a full range of mixity to be used for design purposes.

This global phase angle for a specific geometry is defined in terms of the stress intensity factors[3]:

$$\psi = \tan^{-1}\left(\frac{K_{II}}{K_I}\right) \tag{3}$$

where K_I and K_{II} are the mode I and mode II stress intensity factors, respectively. Once geometries are chosen, this parameter can be calculated for a variety of adherend thicknesses and moduli to determine an appropriate test setup.

Lai and Dillard applied these equations to common test geometries and the results were shown in the form of a comparison. The three geometries that are of interest in this research are the double cantilever beam (DCB), end loaded split (ELS), and four point bend (FPB, similar to the SLB geometry) geometries, as they are most relevant to the testing of adhesively bonded joints. The fracture efficiencies and phase angles for these geometries, assuming symmetric adherends, are shown in Table 2.1.

Table 2.1. Fracture efficiencies and phase angles of common test geometries[3]

	DCB	ELS	FPB
T_e	$\frac{1}{3}\frac{h}{E}$	$\frac{1}{4}\frac{h}{E}$	$\frac{7}{48}\frac{h}{E}$
ψ	0°	90°	40°

A useful method for determining mode mixities due to variable adherend thicknesses and moduli is presented by Hutchinson and Suo[4]. This method uses the moments and forces present near the crack tip to determine the energy release rate, mode mixity, and a variety of other parameters for any chosen geometry. Each geometry is simply defined by the unique moments and forces inherent in the specimen design. The authors define several basic moments and forces applied to a specimen depending on the

specimen geometry and loading configuration. These parameters are shown in Figure 2.4.

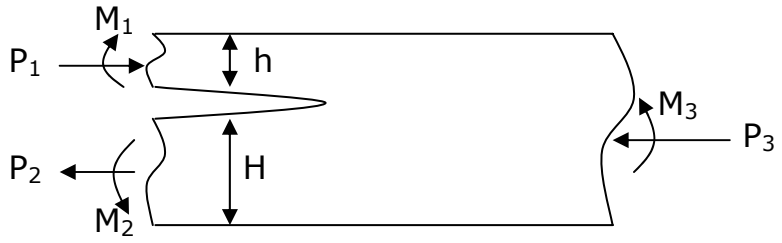

Figure 2.4. Moments and forces for Hutchinson and Suo analysis[4]

This figure is the basis for a set of equations, given in Appendix A, that can be used to calculate stress intensity factors and energy release rates for a variety of loading conditions. Although the figure shows a homogeneous material, this model can be applied to adhesive joints in cases where the adhesive layer can be ignored for analysis purposes[4].

2.2: Temporal Crack Stability

Temporal crack stability is of great importance, especially when working with brittle adhesives like epoxies due to the nature of these materials. The two main types of crack growth are stable and unstable. Stable growth is characterized by the crack propagating in a steady, continuous manner, with the load remaining relatively constant[5]. In this case, the rate of crack growth is dependent on the loading rate employed. Unstable, or stick-slip, crack growth is characterized by the crack jumping from arrest point to arrest point with no direct correlation between the test rate and crack growth rate[5]. Yamini and Young describe this "stick-slip" process as slow growth through the plastic zone (stick) followed by rapid growth through virgin material ahead of the plastic zone (slip)[6]. Many theories have been presented to explain stick-slip growth, attributing

this behavior to specimen geometry, test condition, load train compliance, and adhesive property effects[7, 8, 6, 9, 5].

For unstable growth, the concept of crack arrest is very controversial. Two separate views exist on this topic. Many researchers claim that the arrest energy release rate is a direct result of the adhesive properties, thus the value is calculated using a static analysis. Others claim that in unstable growth, dynamic effects must be considered due to stress waves and structural vibrations that occur as the crack accelerates and gains kinetic energy, which in turn affects the crack arrest as predicted by the concept of recovered kinetic energy[5]. For the purposes of this thesis, only initiation energy release rates will be considered to provide simplicity in the presentation of test results and because these arrest values were believed to be less meaningful in the tests conducted.

2.2.1: Fracture Process Zone Effects

The fracture process zone at the crack tip greatly influences the behavior of the crack as it grows through an adhesive. The manner of propagation within a given adhesive is dependent on the amount of plastic deformation as a result of yielding at the crack tip[5]. This rate dependent yielding is a result of the viscoelastic time dependence of the adhesive. If there is significant plastic deformation, the crack tip will blunt and the amount of energy stored will exceed the amount necessary for stable propagation, causing the crack to jump once it has propagated through the yielded zone[5]. Phillips et al. observed crack tip blunting in an epoxy loaded in double torsion[7]. As the load was increased the crack tip blunted until the crack propagated in a stick-slip fashion, at which point a sharp crack tip again formed.

Kinloch and Williams also discussed crack tip blunting and its effects, and developed a model for the degree of blunting at the crack tip in an epoxy[9]. This model is presented in Appendix B. They tested both bulk double torsion and compact tension geometries as well as bonded tapered double-cantilever beam specimens[9]. According to Kinloch and Williams, the degree of blunting influences both the fracture toughness and the mode of crack growth. They define two stress intensity factors, the first relating to the value necessary for the onset of growth for a sharp crack, K_{Ic}, and the second correlating to the value for the onset of growth for a blunt crack, K_{Ib}[9]. Since they are proportional, these stress intensity factors will be defined in terms of the energy release rates G_{Ic} and G_{Ib} for the purposes of this thesis so that they can be directly correlated to test data. For stable growth $G_{Ic} \approx G_{Ib}$, and thus $G_{Ib}/G_{Ic} \approx 1$. For unstable crack growth, G_{Ib} represents the initiation energy release rate and is greater than G_{Ic}, which represents the arrest value, which Kinloch and Williams found to be approximately equal to the initiation value for stable growth[9]. In the unstable growth case, the greater the ratio G_{Ib}/G_{Ic}, the greater the crack jump distance, as well as the plastic zone size. Gledhill and Kinloch studied both stable and unstable crack growth and found that for continuous, stable growth, G_{Ic} was approximately independent of crack velocity, while for unstable growth G_{Ib} increased significantly with velocity in tapered double-cantilever beam specimens[5]. In their testing, Gledhill and Kinloch found crack velocities of 10^{-4} to 5 m/s for stable growth, and velocities of 20 to 450 m/s for unstable growth.

2.2.2: Fracture Surfaces

Stable and unstable crack growth produce very different fracture surfaces. Yamini and Young found that stable growth in a bulk epoxy tested in double torsion

produced a smooth fracture surface, whereas unstable growth produced rough fracture regions at crack arrest points[8]. Using a Talysurf device, they determined that the intensity and roughness of these regions was determined by the distance the crack jumped from the previous arrest point. They correlated these large crack jumps and well-defined plastic zones to points with high energy release rate values; specifically, large jumps occurred when the initiation energy release rate was much larger than that of the arrest[6,8]. Kinloch and Williams also found that higher initiation energy release rates led to larger plastic zone sizes[9].

According to Yamini and Young, surface patterns in epoxies that are a result of unstable crack growth fall into three main categories: fine arrest lines perpendicular to the direction of propagation, triangular markings in the direction of propagation, and broad rough regions also perpendicular to the propagation direction[6]. The existence of each feature on the surface depends mainly on the test temperature and the degree of cure of the adhesive used. Triangular markings are indicative of an under-cured epoxy and generally have an underlying nodular structure with a magnitude of approximately 100 nm[6]. Fine arrest lines are a result of propagation just past the transition from stable to unstable growth, and have a nodular structure on the order of 50 nm. Finally, the broad rough regions are created by plastic deformation at the crack tip as a result of unstable growth in a well cured specimen[6].

Yamini and Young found that the size of the slow growth region formed by the plastic deformation at the crack tip is approximately the same as the Dugdale plastic zone radius, calculated as:

$$r_p = \frac{\pi}{8}\left(\frac{K_{IC}}{\sigma_y}\right)^2 \qquad (4)$$

where σ_y is the yield stress of the material, and K_{IC} is the critical mode I stress intensity factor[6]. This finding indicates that a Dugdale plastic zone may be present at the crack tip immediately prior to propagation, as a result of the slow propagation due to plastic deformation[6].

2.2.3: Temperature and Rate Effects

In many cases, significant differences are found with identical specimens tested at different rates or temperatures. A representation of the effects of these parameters on the energy release rate is shown in Figure 2.5. As temperature is decreased or the log of the rate is increased into the region on the backside of the curve, unstable growth occurs. The onset of this unstable region is dependent on the properties of the chosen materials.

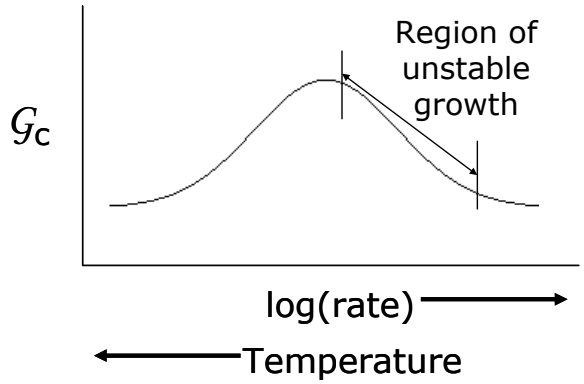

Figure 2.5. Relation of energy release rate to temperature and test rate

In epoxies, the yield stress decreases with increasing temperature or decreased strain rate, allowing for greater plastic deformation and thus, unstable crack propagation[9]. Propagation is more likely to be stable at lower temperatures, when the material is well below its T_g[6]. Phillips et al. found that for their system, initiation energy release rates were higher at lower test rates and higher temperatures up to 22°C[7]. They also found that the initiation energy was rate dependent, but the arrest energy was independent of loading

rate. This lack of rate dependency in arrest energy release rates was also observed by Yamini and Young[8].

Yamini and Young also found that the plastic zone size increased when temperature was increased from -60 to 60°C, leading to larger crack jumps and higher initiation energy release rates at the higher temperatures[8]. Arrest values were unobtainable at higher temperatures, as cracks propagated along the entire specimen without arresting. The fracture surfaces of these higher temperature tests depicted broad, rough hackled regions, evident of a large plastic zone[8].

2.2.4: Adhesive Curing Effects

Crack stability has also been found to be dependent on the makeup of the adhesive used, particularly the curing agent, as well as the manner in which test specimens are cured[8]. Phillips et al. found significant differences in fracture energies as well as surface morphologies between adhesives cured with primary amines and mixed amines[7]. Yamini and Young found increased initiation energy release rates as well as larger crack jumps as the curing agent content was increased[8]. The arrest energy release rates, however, remained relatively constant regardless of curing agent content. As the amount of curing agent was increased, broader, more defined plastic zones were found on the fracture surfaces, also indicating an increase in toughness[8].

The curing temperature is also said to greatly affect the manner of crack propagation. Yamini and Young used post-curing temperatures up to 150°C on their double torsion bulk specimens, and found larger crack jumps and higher initiation energy release rates at post-cure temperatures above 100°C[8]. Again, here the arrest energy release rate was constant, regardless of post-cure temperature. They also found that a

longer post-cure period, up to 3 hours, produced larger crack jumps between arrest points[8].

In conclusion, it seems that the manner of crack propagation is strongly influenced by specimen geometry, test temperature and rate, and the curing time and temperature. Now that general information that applies to all geometries has been given, each geometry will be covered in depth. Dynamic effects due to high test rates will also be discussed for each geometry, as they are an important factor in impact loading.

2.3: Mode I

Mode I testing is the most widely used form of fracture testing because of simplicity in specimen preparation, test setup, and data analysis. The most common and widely accepted geometry for determining mode I energy release rate values is the double cantilever beam (DCB). This is mainly because of the simplicity of the test setup and data collection. Figure 2.1 shows a schematic of this geometry and some relevant parameters to be discussed in this section.

DCB tests come in two varieties, standard and tapered. The standard DCB is the most common specimen due to its simplicity and ease of use. One issue with this test, as with any fracture test, is that the slope of the compliance changes as the crack propagates along the specimen. The tapered DCB was developed to provide a constant value for the slope of the compliance as the crack grew within the specimen, but is not often used because of added cost and complexity associated with cutting the taper into the adherends[4]. Advances in technology have reduced the need for the tapered specimen as the compliance change can readily be incorporated into the analysis and computer control of the test frame, although this geometry is still advocated by some[10].

2.3.1: Analysis

As mentioned before, there are many analysis methods available for analyzing DCB data. Many of these methods are based on the calculated compliance of the DCB specimen. The compliance is defined as the opening displacement (Δ in Figure 2.1) measured at the load application points divided by the applied load. Many of the compliance methods are based upon the expression (assuming a linear load-deflection relation):

$$G_{Ic} = \frac{P_c^{\,2}}{2B}\frac{dC}{da}, \tag{5}$$

developed by Irwin and Kies[11], where P_c is the critical load, B is the width, C is the compliance, and a is the crack length. These variables represent the same parameters in each case that will be presented.

A widely used beam theory method, presented by Blackman et al., is the corrected beam theory approach, which not only takes into account the crack tip effects and shear deformations, but also corrects for large beam deflections[12]:

$$G_{Ic} = \frac{12FP_c^{\,2}(a+\chi_1 h)^2}{B^2 h^3 E_f} \tag{6}$$

where F is a correction for large deflections:

$$F = 1 - \theta_1(\Delta / L)^2 - \theta_2(\Delta l_1 / L)^2 \tag{7}$$

where $\theta_1 = 0.3$, $\theta_2 = 1.5$, and l_1 is the distance of the load point above the beam axis. The variable χ_1 accounts for the root rotation and deflection at the crack tip and is deduced by taking the intercept of a plot of $(C/N)^{1/3}$ versus crack length, where N, a correction factor for stiffening due to the end blocks, is defined by the equation:

$$N = 1 - \theta_3(l_2 / L)^3 - \theta_4(\Delta l_1 / L^2) - \theta_5(\Delta / L)^2 \tag{8}$$

where $\theta_3 = 1$, $\theta_4 = 1.125[1-(l_2/a)^2]$, $\theta_5 = 0.257$, and l_2 is the half-width of the end block[12].

2.3.2: Dynamic Effects

Many of the compliance based methods work well for quasi-static testing, but the introduction of dynamic loading creates issues involving load measurement. The propagation of shear and bending waves along the specimen due to dynamic loading creates resonance in load cells, making load signals too noisy to obtain valid data[13]. Because of this phenomenon, Blackman et al. have developed a modified analysis method for the DCB geometry that does not require direct measurement of the load[12]:

$$G_{Ic} = \frac{3}{16}\frac{F}{N^2}\frac{\Delta_c{}^2 h^3 E_f}{(a+\chi_1 h)^4} \tag{9}$$

where F and N are corrections for end block effects and large deformations, and as before, χ_1 accounts for the root rotation and deflection at the crack tip and is obtained by taking the intercept of the plot of $(C/N)^{1/3}$ versus crack length[13]. This method eliminates the dynamic issues arising from erratic load measurements, but does not account for kinetic energy effects found in high rate testing.

To account for kinetic energy, a dynamic analysis must be conducted to include dynamic and transient effects[13]. This method is not often used due to its complexity and additional analysis time. Blackman et al. present a dynamic analysis method and compare results calculated using this method to results obtained from static analyses[13]. The dynamic portion of the analysis is based on a Berry method approximation, as an exact solution is not feasible in most cases due to the nature of the equation of motion.

Their analysis is broken into three portions based on the state of the crack growth. The first, pre-initiation, is a straightforward energy calculation because there is no

contribution to the kinetic energy from the crack motion[13]. Once there is steady state propagation, the kinetic energy can be calculated based on a previously defined kinetic energy term as well as the velocity contribution from the crack motion, and from this the energy release rate can be determined. Finally, there is a transient region between the pre-initiation and steady state regions. This region is characterized using a small perturbation method that is an approximation of the transient contribution of the kinetic energy. This transitory region makes the greatest contribution to the dynamic effects from high test rates[13]. The exact rate at which these dynamic analyses should be used is unknown, as material properties are also a large contributor to dynamic effects. Results calculated without these corrections result in conservative estimations, thus many researchers choose to ignore them[13].

2.4: Mode II

Another loading mode that is very important in fracture characterization is mode II, the pure forward shearing mode. This type of loading is characterized by the idea of two plates sliding past one another, often causing a hackled fracture pattern within the specimen as a result of the shear deformations[1]. Mode II loading is very important because shear is one of the predominant load types found within bonded structures[14]. Adhesives are commonly used in shear-dominated rather than peel-dominated joints for better structural performance.

As mentioned before, the ENF and ELS geometries are widely used for the characterization of mode II fracture properties. A schematic for each is shown in Figures 2.2 and 2.3 respectively. The parameters shown will be discussed in detail later in this section.

2.4.1: Analysis

Wang and Williams proposed a compliance-based method derived from beam theory for determining energy release rate values for the ELS geometry[15]. This analysis method is similar to those previously discussed for the double cantilever beam test and includes similar correction factors for the crack length, a. The difference here is that in mode II loading, both beams are bent in the same direction, as opposed to being bent in opposite directions in mode I loading. As a result, the value of the mode II correction for the root rotation and deflection at the crack tip, χ_{11}, is expected to be less than that of χ_1, the mode I correction factor[15].

In the case of mode II analysis, the use of a beam theory approach provides a means to calculate energy release rates from test data. Wang and Williams define the mode II energy release rate for the ELS geometry as:

$$G_{II_{ELS}} = \frac{9P^2(a+\chi h)^2}{4B^2h^3E_f} \tag{10}$$

where P is the applied load, a is the measured crack length, h is the adherend thickness, and B is the specimen width. As previously discussed, χ accounts for the root rotation and deflection at the crack tip and is determined from both the measured compliance and the compliance at zero crack length (C_0) using the equation[15]:

$$C - C_0 = \frac{3(a+\chi h)^3}{2Bh^3E_f} \tag{11}$$

These equations were also verified using a semi-empirical finite element method and agreement in energy release rate was found to be within 4%[15].

Wang and Vu-Khanh state that the ELS test is more suitable for determining mode II fracture properties as it is more conducive than the ENF geometry to stable crack

growth[14]. This is due to a longer available beam length for crack extension. Because of these factors, the ELS geometry was chosen for this research to characterize mode II fracture and will be the focus of the rest of this section.

2.4.2: ELS Issues

When using tough materials such as composites and toughened adhesives, large deflection effects become problematic in the ELS geometry. With tougher materials, a larger deflection is needed to initiate a crack, thus creating a nonlinear relationship between the measured load and displacement[14]. This causes the previously defined compliance and energy release rate equations (Equations 10 and 11) to be no longer valid without corrections. Also, the damage zone at the crack tip and the fact that the beams travel in the same direction and thus the crack does not open, make it hard to identify exactly where the crack tip is within the specimen[14].

Wang and Vu-Khahn have developed an effective crack length to take the damage zone into account when calculating fracture toughness[14]. This method uses the variation of the compliance with crack length to determine an effective crack length based on the equation:

$$C = \frac{12}{Bh^3 E_f}\left(a^3 + \frac{L^3}{3}\right) \tag{12}$$

where B is the specimen width, h is the adherend thickness, L is the beam span, and a is the measured crack length[14]. The effective crack length is determined by substituting the secant compliance into this equation and solving for a.

This approach is only valid for small deflections, because nonlinearity in load deflection curves for large deflection cases include not only the damage zone effects, but

also the large deflection effect[14]. In this case the effective crack length can be determined by an interpolation of a normalized load versus normalized deflection plot, where the normalized load is defined by the equation:

$$\overline{P} = \frac{PL^2}{E_f I} \tag{13}$$

and the normalized deflection is defined by:

$$\overline{\Delta} = \frac{\Delta}{L} \tag{14}$$

where P, L, and E_f are as previously defined, and I is the second moment of area of one of the adherends[14].

Because of the various issues with load measurement, Blackman et al. developed an analysis method based on displacements rather than a measured load[16]. This eliminates the effects of the load rotation and the nonlinearity of the load deflection curve[17]. With this method, the energy release rate is calculated using the equation:

$$G_{II} = \frac{9\Delta^2 h^3 E_f (a + \chi_{11} h)^2}{[3(a + \chi_{11} h)^3 + (L + 2\chi_1 h)^3]^2} \frac{F}{N^2} \tag{15}$$

where F and N are once again end block corrections, and as before χ_1 is the mode I correction for rotation and deflection at the crack tip. A new correction factor, χ_{11}, is also introduced as the mode II correction for rotation and deflection at the crack tip[16].

2.4.3: Dynamic and Unstable Propagation Effects

In dynamic testing, many issues arise in regard to crack stability. The large deflections required for crack initiation can result in unstable crack growth[14]. This unstable, or stick-slip growth is indicated by the crack accelerating and decelerating, and

in some cases arresting, within the material. Blackman et al. also found that higher test rates (>3.3E^{-5} m/s) contributed to unstable growth.

Along with material property effects, many researchers have also found that specimen geometry has an effect on crack stability for both quasi-static and dynamic testing. Wang and Vu-Khahn found that there is a critical crack length that defines the transition between unstable and stable growth for the ELS geometry[14]. Using energy methods, Goyal predicts that this critical crack length, which the precrack must be greater than to promote stable propagation, is 0.55L, where L is the beam span[18]. Wang and Vu-Khahn used a linear beam theory approach and arrived at the same result for this value[14]. They also conducted fracture tests and observed that crack growth was stable beyond a crack length of approximately 0.49L. Blackman et al. chose an initial crack length of 0.6L to ensure stable crack growth throughout the measurement region[16].

Blackman et al. also present results on the topic of static and dynamic analysis of fracture data[16]. This is very important in dynamic testing, as all of the aforementioned analysis methods are static based and do not include any dynamic effects associated with the added kinetic energy. Blackman et al. found that the static methods obtained energy release rate values within 3% of those calculated using a dynamic analysis method for test rates up to 3 m/s for the geometries and systems they studied. They concluded that for rates at or below this level, static analysis methods are sufficient for obtaining energy release rate values[16].

2.5: Mixed-Mode I/II

Mixed-mode fracture data is also important in the creation of fracture failure envelopes, as this type of data defines the region between mode I and mode II. This type

of loading induces a mixture of both opening and shearing modes, giving results that lie between the pure mode I and II data. Mixed-mode loading is very important in design because joints are rarely subjected to pure shear or pure opening, but usually a combination of the two, as well as mode III, which will not be discussed in this thesis[19]. This is due to loading mode as well as dissimilar materials and thicknesses of materials being bonded together, thus forming asymmetry within the joint and causing a mixed loading condition[20].

Many geometries are available to determine these mixed-mode fracture energies, some of which are simply variations on geometries developed for mode I and II testing. These geometries include the mixed-mode bending (MMB) geometry; the single leg bend geometry (SLB); the asymmetric DCB (ADCB), a variation of the DCB with adherends of different thicknesses; and the asymmetric end-notched flexure geometry (AENF), an asymmetric form of the geometry shown in Figure 2.3[21]. As with the symmetric case, the AENF can also be configured as an end-loaded split geometry with asymmetric adherends.

The mixed-mode bending geometry is a frequently used method for obtaining mixed-mode fracture data[22]. This geometry allows for many combinations of mode I and II loading, and is simply a superposition of the DCB and ENF geometries[23]. One issue with this geometry is that a geometrically nonlinear analysis is preferable for bimaterial specimens, adding considerable complexity to the measurement and analysis process[22]. Another variation of this type of fixture, which also allows for a full range of mode mixities, was presented by Fernlund and Spelt[24]. Because they allow for a full range of mode mixities, these types of tests are very desirable for quasi-static fracture testing.

Unfortunately, the design and complexity of the required fixturing does not lend itself to impact loading. As a result, neither test type was used for the purposes of this research.

The single leg bend, also known as the mixed-mode bend, geometry is shown in Figure 2.6. Load is applied to the longer beam, thus causing opening and shearing between the adherends. The crack length, a, opening displacement (measured from the original bond plane), Δ, length, L, and adherend thickness, h are defined as before.

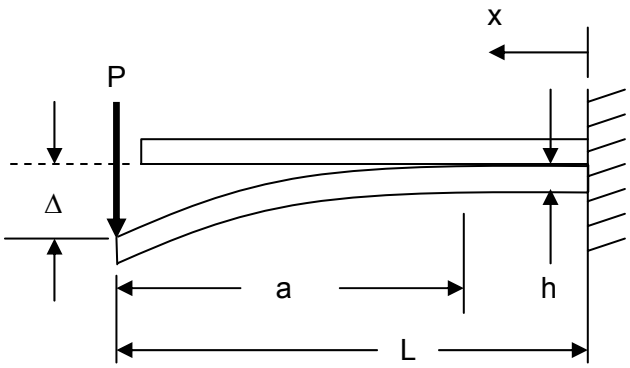

Figure 2.6. Single leg bend geometry

According to Davidson and Sundararaman, this geometry is frequently used because it[22]:

- can accommodate a wide variety of material pairs
- is relatively easy and inexpensive to manufacture, and
- does not require an extensive analytical or numerical approach to analyze test data.

The ADCB geometry is also commonly used as it can be tested in the same manner as the standard DCB geometry, and as with the DCB, the ADCB specimens are also simple to fabricate[25]. This geometry also provides a reasonable range of mode mixity and allows for the trajectory of the crack to be controlled[26]. The AENF is also widely used as this geometry provides simplicity in setup and analysis as well[21].

2.5.1: Analysis

Charalambides et al. developed a general failure criteria for mixed-mode fracture[27]. This criteria assumes that a crack loaded globally in modes I and II will have a resulting mode I component equal to the failure value G_0, which is defined as:

$$G_0 = G_c[\cos^2(\psi - \psi_0) + \sin^2(\omega)\sin^2(\psi - \psi_0)] \tag{16}$$

where G_c is the measured fracture energy, ω is the slope of the surface roughness, and ψ is the phase angle[27]. ψ_0 is based on the elastic mismatch and is equal to zero when adherends are elastically identical, and ω=0 for smooth fracture surfaces. The basic parameters, G_0, ω, and ψ_0, can be determined by using the aforementioned equation along with the equations:

$$\sin^2(\omega) = \frac{G_0}{G_{Ic}} + \frac{G_0}{G_{IIc}} - 1 \tag{17}$$

$$\tan^2(\psi_0) = \frac{1 - \dfrac{G_0}{G_{Ic}}}{1 - \dfrac{G_0}{G_{IIc}}} \tag{18}$$

where G_{Ic}, G_{IIc} are experimental observations of fracture energies that can be readily measured[27]. This method has been successfully used by Blackman et al. to provide a fit to experimentally determined failure loci[16].

Critical energy release rate values can be directly calculated for the ADCB geometry by the use of equations derived from elastic beam theory[26]. This method models the specimen as two elastic cantilever beams and uses the derivative of the strain energy stored in the beams to determine the energy release rate through the equation:

$$G = \frac{3\Delta^2 E_1 E_2 h_1^{\,3} h_2^{\,3}}{8a^4(E_1 h_1^{\,3} + E_2 h_2^{\,3})} \tag{19}$$

where E_1, E_2, h_1, and h_2 are the elastic moduli and thicknesses of the adherends, a is the crack length, and Δ is the opening displacement. This equation is adequate for crack lengths that are much longer than the beam thickness, but this simple beam model may be too stiff to accurately capture the energy release rate for short specimens[26]. As a result, Kanninen's beam on elastic foundation model was applied to obtain the equation:

$$G = \frac{3\Delta^2 E_1 E_2 h_1^3 h_2^3 (C_1^2 E_2 h_2^3 + C_2^2 E_1 h_1^3)}{8a^4 (C_2^3 E_1 h_1^3 + C_1^3 E_2 h_2^3)} \tag{20}$$

where $C_1 = 1+0.064*h_1/a$ and $C_2 = 1+0.064*h_2/a$. This method has been found to provide a better correlation between fracture data[26].

Ducept et al. explored the differences between global and local methods of analysis and the implications of each[23]. The global approach uses beam theory to determine a total energy release rate. The mode II release rate is then determined by assuming that under pure mode II loading, the curvature in the two arms is the same. The mode I release rate can then be determined using the relationship[23]:

$$G = G_I + G_{II} \tag{21}$$

Ducept et al. found, surprisingly, that this method predicted pure mode I loading regardless of adherend thickness mismatch. As a result, this method is not recommended for the ADCB geometry[23]. The local method for determining energy release rate values for the ADCB geometry is based on a stress intensity factor calculation[23].

As previously mentioned, the global method always predicted mode I loading and did not produce useful results. The local method predicts mixed-mode loading similar to that found in finite element results, but does generate somewhat different G_I/G_{II} ratios. As a result of these findings, Ducept et al. recommend using the local analysis method, verifying the results with a finite element analysis[23].

More advanced methods have also been developed to determine fracture energies for the ADCB geometry. Guo and Weitsman present a method that utilizes Green's functions for shear deformable bodies that allows for the evaluation of G_I and G_2 without the use of finite elements[20]. This essentially one-dimensional approximation gives a simple engineering approach and agrees with finite element results within 5%. Interlaminar stresses, deflections, and the total energy release rate can also be calculated. Larger disparities are found between the model and finite element results in the deflection data, possibly due to the limitations of beam theory, but these have little effect on the energy release rate values[20]. This method provides a simplified, one-dimensional approach to determine fracture energies from the ADCB geometry, but does not include information regarding crack initiation, growth, and stability.

2.5.2: Dynamic Considerations

As with the other geometries, dynamic loading of mixed-mode geometries also creates issues with load measurement. Because of this, Blackman et al. provide a displacement based solution for the fixed-ratio mixed-mode geometry, where the mode I and II energy release rates are defined as:

$$G_I = \frac{12\Delta^2 h^3 E_f (a + \chi_1 h)^2}{[7(a + \chi_{11} h)^3 + (L + 2\chi_1 h)^3]^2} \frac{F}{N^2} \tag{22}$$

$$G_{II} = \frac{9\Delta^2 h^3 E_f (a + \chi_{11} h)^2}{[7(a + \chi_{11} h)^3 + (L + 2\chi_1 h)^3]^2} \frac{F}{N^2} \tag{23}$$

where $\chi_{II} = 0.42\chi_I$, and all other parameters are as previously defined[16]. As with the ELS geometry, this analysis is static, not including kinetic energy effects. Energy release rate values calculated with this equation were found to be within 3% of those calculated using dynamic methods for test rates of up to 3m/s[16]. This method can also be applied to

the ADCB and AENF geometries by modifying the equations derived for the symmetric cases to incorporate asymmetric beam thicknesses and elastic moduli.

Crack stability is also an issue with mixed mode fracture. Blackman et al. found that stable growth could be obtained with crack lengths that were greater than 0.6 times the beam span[16].

2.6: Conclusion

All of the prescribed geometries and methods can be used to determine fracture properties of a variety of adhesive systems to generate fracture failure envelopes to be used for design. The available mode-mixity provides real-world information that can be used to accurately predict the fracture behavior of adhesive joints. Dynamic considerations such as kinetic energy effects and crack stability are also important in higher rate tests, as they may have a large effect on the way data is collected and analyzed.

Due to available equipment and resources, the DCB, ELS, and SLB geometries were chosen to characterize the mode I, II, and mixed-mode I/II behavior of the adhesive/composite system. Standard beam theory methods were chosen as methods of analysis, as they have been found to be both time efficient and reliable in previous experimentation. Bondline thickness and test geometry have been taken into consideration to reduce the effects of unstable crack growth, and fracture surfaces are to be analyzed to detect differences between static and dynamic specimens.

References

1. O'Brien, K.T., "Interlaminar fracture toughness: the long and winding road to standardization," *Composites Part B*, **29B** (1998), 57-62.
2. Martin, R.H., "Interlaminar fracture characterization: a current review," *NASA Contractor Report 187573*, July 1991.
3. Lai, Y.-H., Dillard, D.A., "Using the fracture efficiency to compare adhesion tests," *International Journal of Solids Structures,* **4** (1997), 509-525.
4. Hutchinson, J.W., Suo, Z., "Mixed mode cracking in layered materials," *Advances in Applied Mechanics*, **29** (1992), 63-189.
5. Gledhill, R.A., Kinloch, A.J. "Mechanics of crack growth in epoxide resins," *Polymer Engineering and Science*, **19**, No. 2 (1979), 82-88.
6. Yamini, S., Young, R.J., "The mechanical properties of epoxy resins part II: Effect of plastic deformation upon crack propagation," *Journal of Materials Science*, **15** (1980), 1823-1831.
7. Phillips, D.C., Scott, J.M., Jones, M., "Crack propagation in amine-cured epoxide resin," *Journal of Materials Science*, **13** (1978), 311-322.
8. Yamini, S., Young, R.J., "Crack propagation in and fractography of epoxy resins," *Journal of Materials Science*, **14** (1979), 1609-1618.
9. Kinloch, A.J., Williams, J.G., "Crack blunting mechanisms in polymers," *Journal of Materials Science*, **15** (1980), 987-996.
10. Blackman, B. R. K., Hadavinia, H., Kinloch, A.J., Paraschi, M., Williams, J.G., "The calculation of adhesive fracture energies in mode I: revisiting the tapered double cantilever beam (TDCB) test," *Engineering Fracture Mechanics*, **70** (2003), 233-248.

11. Irwin, G.R., Kies, J.A., "Critical energy rate analysis of fracture strength," *Welding Journal,* **33** (1994)**,** 193–198.
12. Blackman, B.R.K., Dear, J.P., Kinloch, A.J., Macgillivray, H., Wang, Y., Williams, J.G., Yayla, P., "The failure of fibre composites and adhesively bonded fibre composites under high rates of test. Part I: mode I loading-experimental studies," *Journal of Materials Science*, **30** (1995), 5885-5900.
13. Blackman, B.R.K., Dear, J.P., Kinloch, A.J., Macgillivray, H., Wang, Y., Williams, J.G., Yayla, P., "The failure of fibre composites and adhesively bonded fibre composites under high rates of test. Part II: mode I loading—dynamic effects," *Journal of Materials Science*, **31** (1996), 4451-4466.
14. Wang, Y., Vu-Khanh, T., "Use of end-loaded-split (ELS) test to study stable fracture behavior of composites under mode II loading," *Composite Structures*, **36** (1996), 71-79.
15. Wang, Y., Williams, J.G., "Corrections for mode II fracture toughness specimens of composites materials," *Composites Science and Technology*, **43** (1992), 251-256.
16. Blackman, B.R.K., Dear, J.P., Kinloch, A.J., Macgillivray, H., Wang, Y., Williams, J.G., Yayla, P., "The failure of fibre composites and adhesively bonded fibre composites under high rates of test. Part III: mixed-mode I/II and mode II loadings," *Journal of Materials Science*, **31** (1996), 4467-4477.
17. Kinloch, A.J., Wang, Y., Williams, J.G., Yayla, P., "The mixed-mode delamination of fibre composite materials," *Composites Science and Technology*, **47** (1993), 225-237.
18. Goyal, V.K. " Analytical modeling of the mechanics of nucleation and growth of cracks." Dissertation, Virginia Tech, Blacksburg, VA, 2002.

19. Parvatareddy, H., Dillard, D.A., “Effect of mode-mixity on the fracture toughness of Ti-6Al-4V/FM-5 adhesive joints,” *International Journal of Fracture*, **96** (1999), 215-228.

20. Guo, Y.-J., Weitsman, Y.J., “A modified DCB specimen to determine mixed mode fracture toughness of adhesives,” *Engineering Fracture Mechanics*, **68** (2001), 1647-1668.

21. Sundararaman, V., Davidson, B.D., "New test methods for determining fracture toughness as a function of mode mix for bimaterial interfaces," *Application of Fracture Mechanics in Electronic Packaging and Materials*, ASME **64** (1995), 141-154.

22. Davidson, B.D., Sundararaman, V., "A single leg bending test for interfacial fracture toughness determination," *International Journal of Fracture*, **78** (1996), 193-210.

23. Ducept, F., Gamby, D., Davies, P., “A mixed-mode failure criterion derived from tests on symmetric and asymmetric specimens,” *Composites Science and Technology*, **59** (1999), 609-619.

24. Fernlund, G., Spelt, J. K., “Mixed-mode fracture characterization of adhesive joints,” *Composites Science and Technology,* **50** (1994), 441-449.

25. Maugis, D. *Contact, Adhesion, and Rupture of Elastic Solids*. New York: Springer, 2000.

26. Xiao, F., Hui, C.-Y., Kramer, E.J., “Analysis of a mixed mode fracture specimen: the asymmetric double cantilever beam,” *Journal of Materials Science*, **28** (1993), 5620-5629.

27. Charalambides, M., Kinloch, A.J., Wang, Y., Williams, J.G., “On the analysis of mixed-mode fracture,” *International Journal of Fracture*, **54** (1992), 269-291.

Chapter 3: Specimen Preparation and Test Methods

This section will discuss the preparation of test specimens used for the purposes of this thesis as well as the methods used to test them. The materials used for these tests will be covered, as well as the methods used to bond them into beam specimens. Test methods will then be presented for mode I, II, and mixed-mode I/II fracture characterization.

3.1: Materials

The material choices for this thesis were based upon future automotive technology, as the purpose of this research was to determine the fracture properties of these materials for automotive applications. A simple bonded-beam specimen, shown in Figure 3.1, was used for each test geometry to add simplicity to the preparation process. Initial crack lengths and loading configurations were then varied to obtain the desired mode mixities.

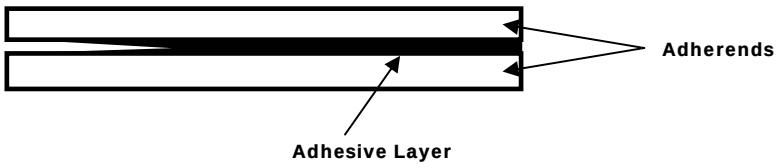

Figure 3.1. Bonded-beam specimen configuration

The chosen adherends were comprised of MTM49/CF0501 woven fiber sheets (T300B-40B) manufactured by Advanced Composites Group (Tulsa, OK) and constructed with 42% resin content by Pacific Composites Inc. (San Clemente, CA). This material is orthotropic, and is a plain weave balanced fabric. This material was received in the form of 625x625 mm panels of several configurations as shown in Table 3.1.

Table 3.1. Composite adherend configurations

Ply Count	Thickness (mm)	Layup Pattern
11	2.5	0/90,±45,0/90, ±45,0/90, ±45,0/90, ±45,0/90, ±45,0/90
12	2.7	0/90, ±45,0/90, ±45,0/90, ±45, ±45,0/90, ±45,0/90, ±45,0/90
20	4.7	0/90, ±45,0/90, ±45,0/90, ±45,0/90, ±45,0/90,45,±45,0/90, ±45,0/90, ±45,0/90, ±45, 0/90, ±45,0/90
36	8.5	0/90, ±45,0/90, ±45,0/90, ±45,0/90, ±45,0/90, ±45,0/90, ±45,0/90, ±45,0/90, ±45,0/90, ±45,0/90, ±45,0/90, ±45,0/90,±45,0/90, ±45,0/90, ±45,0/90, ±45,0/90, ±45,0/90, ±45,0/90

6061 aluminum adherends were also used as a control to provide a means of comparison for the mode I composite data. These adherends measured 25x6.4x254mm and were chemically etched using a P2 process to provide an adequate bonding surface. This process is outlined in Appendix C.

The chosen adhesive was PL731SI, a two-part epoxy system produced by Sovereign Specialty Adhesives Inc. (Buffalo, NY). This adhesive is commercially available and was designed for bonding composites in automotive applications. The adhesive was applied in a mixture ratio of 4:1 using a MixPac DP 200-70 (Salem, NH) pneumatic positive displacement dispensing gun with a regulator pressure of 380 kPa. A 250 mm static mix tube was used to combine the resin and hardener, and the mixture was subsequently dispensed at approximately 1.6 kg/min.

The manufacturer suggests a 2-5 minute cure time at 127°C for full curing. This adhesive has a shelf life of 1 year when stored in a cool dry area, and must not be stored at 7-16°C as crystallization of the curing agent will result. If crystallization occurs due to extended shelf life or storage temperatures, it is recommended that the adhesive be heated for 16 hours at 70°C to remove the crystallization.

3.2: Specimen Preparation

As previously mentioned, all specimens were constructed in a bonded-beam configuration. Aluminum adherends were used in both the static and dynamic DCB configurations, and the composite adherends were used in the static and dynamic DCB, and dynamic ELS and SLB configurations.

In the case of the aluminum adherends, each beam was P2 etched according to the procedure presented in Appendix C to provide an adequate bonding surface. The bondline was then set using either a 0.8 mm or 0.5 mm wire at each end of the specimen. The adherends were sandwiched together and clamped at both ends with standard binder clips. One specimen in each batch was also instrumented with a thermocouple placed at the center of the bondline so that the bondline temperature could be monitored during curing.

Because they were shipped in panel form, the composite adherends were bonded in 300x300 mm sheets. Each surface was abraded with Scotch Brite^{TM} (3M, St. Paul, MN) and then cleaned with acetone prior to bonding. The bondline was again set using either 0.8 mm or 0.5 mm wires at the center and 20 mm from both ends of the composite panels, as shown in Figure 3.2. Initially, these wires were only placed at the ends of the panels, however, this method resulted in inconsistent bondlines due to the adherend flexing. Once the bondline thickness was set, a thermocouple was added to the center of the panel, also shown in Figure 3.2.

Figure 3.2. Bondline thickness wires and thermocouple placement

Approximately 200 mL of adhesive was then applied in a sweeping, continuous manner from one end of the panel to the other. Much care was taken to not cross over previously laid beads as this was found to result in voids within the adhesive layer. Once the adhesive was applied, an upper panel was pressed on, forcing the adhesive towards the panel's edge. Originally, the sandwiched panels were then clamped using large C-clamps at the middle of all four sides. Aluminum plates were also added to the thinner panels (11 and 12 ply) to prevent bowing from the applied force as shown in Figure 3.3.

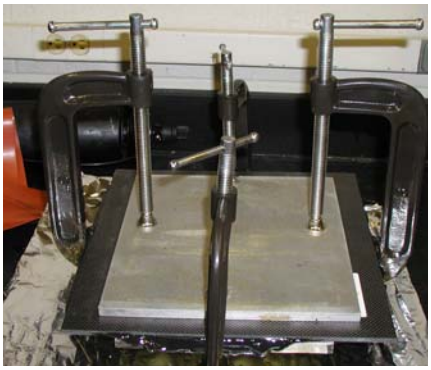

Figure 3.3. Clamping with aluminum plates

Significant bondline thickness variations were found using this method. As a result, a 16" platen press was utilized to provide a more consistent clamping force of approximately 20kN.

Both the aluminum and composite specimens were cured using the same heating process. In each case the specimens or panels were placed in an oven or between platens

set at 210°C to provide as steep a heating gradient as possible to reduce the amount of crystallization prior to curing. A temperature of 210°C was chosen because it was the upper limit of the temperature range of the available equipment. Once the cure temperature of 127°C was reached at the bondline, the specimens were removed from heat and allowed to cool at room temperature. This procedure allowed the specimens to remain within 10°C of the cure temperature for at least 5 minutes (depending on the adherend type and thickness) to ensure full curing. Once cured, the sides of the aluminum specimens were ground on a sanding wheel to remove adhesive spew, and composite specimens were cut into 25x254 mm strips using a Felker (Olathe, Kansas) 41AR saw with a diamond blade and water cooling.

The precracking process used was slightly different for the aluminum and composite specimens. In both cases, a hardened stainless steel wedge was used to drive the crack 50-55 mm into DCB specimens, and 98-100 mm into ELS and SLB specimens to meet the length criteria as previously discussed. Aluminum specimens were precracked at room temperature, but due to the unstable crack growth, a C-clamp was placed at 50mm to force the crack to arrest, at the desired length, as shown in Figure 3.4. Composite specimens were heated in an oven at 200°C for 10 minutes prior to precracking. This method was adopted after issues arose with interlaminar failure within composite adherend specimens. The elevated temperature precrack aids in keeping the precrack within the adhesive layer. Precracks were created using the stainless wedge, but in this case the C-clamp was not necessary as the crack grew stably due to the elevated temperature of the adhesive layer.

Figure 3.4. Aluminum specimen precracking using a C-clamp to force arrests

Once DCB specimens were precracked, size 8-32 holes were drilled and tapped for end blocks in the case of both the aluminum and the composite adherends. A paper ruler was then attached to static DCB specimens for crack length measurement, and Wite-Out® (Milford, CT) typewriter correction fluid was applied to dynamic specimens to provide contrast to aid in edge detection. Both of these methods are shown in Figure 3.5. Due to the test setup, SLB specimens were trimmed prior to precracking such that one adherend was approximately 45 mm longer than the other. The correction fluid was also applied to ELS and SLB specimens, again for edge detection purposes, but because of the loading method, no end blocks were required for these geometries.

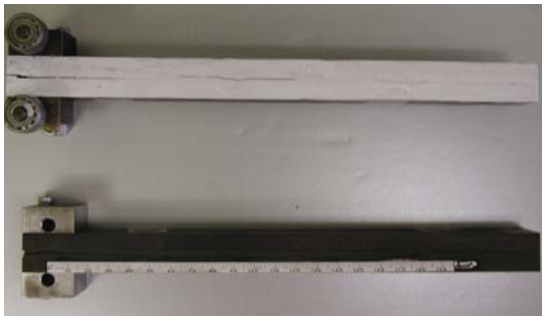

Figure 3.5. Dynamic (top) and static (bottom) DCB specimen configurations

3.3: Static DCB Test Setup

Static double cantilever beam testing was conducted by nominally following ASTM standard D3433. An Instron (Canton, MA) 4500 series test frame with a 5kN

load cell was used for this testing. All data was collected using custom software written with National Instruments LabVIEW^{tm} (Austin, TX). Specimens were loaded into the test frame as shown in Figure 3.6, and a constant opening displacement rate of 1mm/min was used.

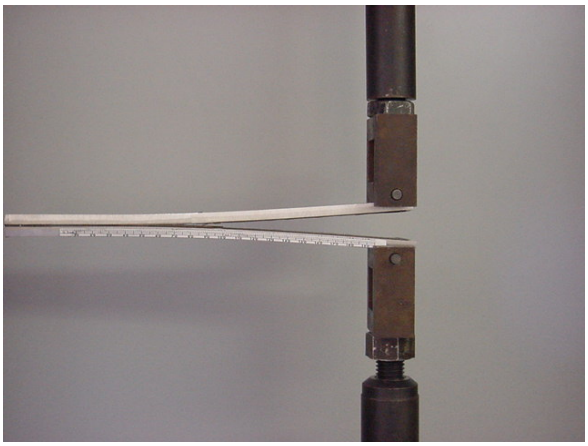

Figure 3.6. Static DCB test configuration during loading

Crack length was measured visually using the paper ruler that was bonded to the specimen during the preparation phase. Load and opening displacement were collected using the Instron's built-in data acquisition system. Upon crack propagation, the load was held (by stopping the crosshead) and the crack length was recorded. The ASTM testing procedure calls for allowing the load to plateau after propagation, but this was not necessary with the chosen adhesive because of the significant load drop as a result of the unstable crack growth. Another deviation from the ASTM method was that specimens were not completely unloaded between crack propagation events to check for plastic deformation in the adherends in the interest of time. Initial testing with each adherend type/thickness showed no indication of adherend deformation and no noticeable deformation was seen on subsequently tested specimens.

3.4: Dynamic Test Setup

All dynamic tests were conducted using a Dynatup (Canton, MA) model 8200 drop tower and Kodak (San Diego, CA) Ecta Pro EM model 1012 high speed imaging system. Each geometry used a custom mounting system that provides the desired loading for each situation. Load was applied in each case by either polycarbonate wedges or a hemispherically-tipped steel tup mounted to the weighted sled on the drop tower, which rides on linear bearings to reduce frictional effects. The sled was dropped from a height of approximately 0.7 meters, reaching a velocity of about 3.8 m/s before striking the specimen.

The Kodak (San Diego, CA) Ecta Pro uses a 192x239 pixel NMOS array with a spectral response of 400 to 1000 nanometers. This system is capable of 256 levels of grey and can store up to 4,800 images. Full frame images can be recorded at rates of up to 1000 frames per second and split frame recording can be done at up to 12,000 frames per second. For dynamic DCB and ELS tests, the record rate was set at 2000 frames per second with an exposure of 1/2000 second to capture as many images as possible, while maintaining an adequate image frame.

3.4.1: Double Cantilever Beam

Dynamic DCB specimens were mounted vertically in the drop tower and tested in a "falling wedge" configuration as shown in Figure 3.7. This "falling wedge" method was originally developed by Shuangyan Xu[1]. Load was applied using two polycarbonate wedges attached to the drop tower sled. These wedges strike ball bearing rollers mounted on pins through the loading blocks, spreading the beams apart and creating mode I loading, as shown in the schematic in Figure 3.7.

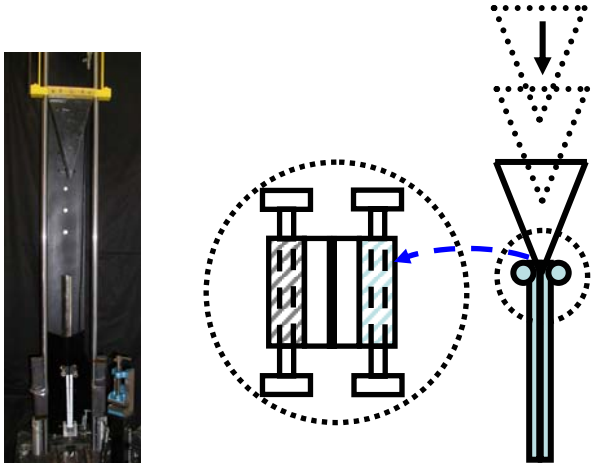

Figure 3.7. Dynamic DCB test configuration

As previously mentioned, all DCB test data was collected visually using the high speed imaging system set at 2000 frames/second. No load or displacement measurements were physically made on the specimen. There were two main reasons this was done for the case of mode I loading. First, as previously referenced from the work of Blackman et al., meaningful load measurement is not possible at high test rates due to wave propagation within test specimens as well as vibration of the adherends. This creates resonances in load cells, causing excessive noise that inhibits collection of meaningful load values. Also, because of the high test rates, crack length cannot be measured in the manner used for static DCB testing due to the rate of crack growth. The displacement profile and opening displacement are deduced from the image data, and all other parameters such as crack length, crack velocity, and energy release rate are calculated in the analysis.

3.4.2: End-Loaded Split

End-loaded split specimens were also tested in the drop tower, but were mounted horizontally in a custom clamping fixture as shown in Figure 3.8. This fixture consists of

a side grooved Palmgren (Chicago, IL) vise mounted to a custom pedestal. The pedestal is constructed of 50x50mm steel box tubing welded to 6.4mm steel plates and is clamped to the drop tower base using 100mm C-clamps. In this case, a hemispherically-tipped steel tup is attached to the drop tower sled and travels downward, striking the end of the specimen as shown in the schematic in Figure 3.8.

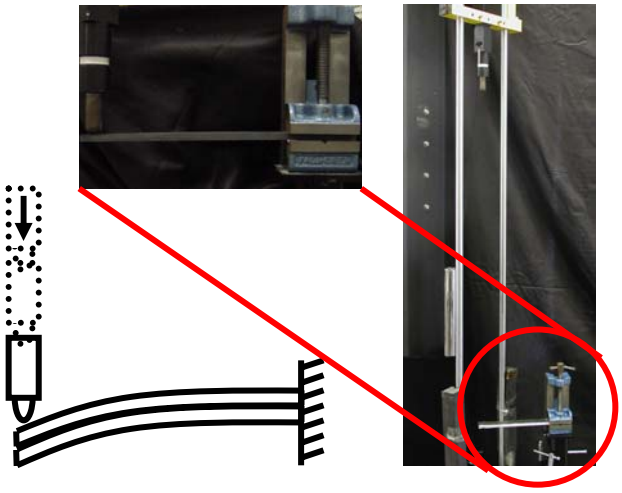

Figure 3.8. Dynamic ELS test configuration

Here, the imaging system is used to collect the displacement profile and end displacement of the specimens. Again, as with the case of the DCB geometry, all other parameters such as crack length and energy release rate are calculated during the analysis phase. Due to the fact that the adherends travel in the same direction, the crack length must be calculated since the crack is not apparent in the collected images.

3.4.3: Single Leg Bend

The single leg bend specimens were also mounted horizontally in the drop tower using the aforementioned fixture, and load was applied using the hemispherically-tipped tup. The difference between the SLB geometry and the ELS geometry is that the SLB uses an adherend length mismatch to vary mode-mixity. To create mixed-mode loading,

one adherend was 45 mm shorter than the other, as previously described. The tup strikes the longer adherend, as shown in the schematic in Figure 3.9, which is mounted on the bottom side, creating both opening and shear loading.

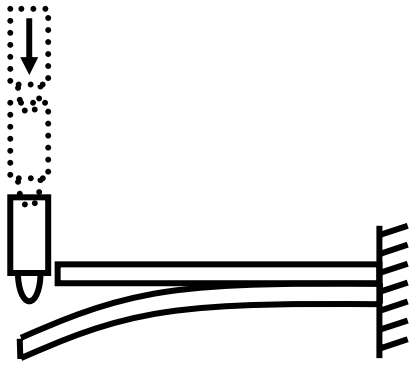

Figure 3.9. Dynamic SLB test configuration

Data collection in this case included the displacement profile as well as the opening displacement, which were both used in determining the crack length. As previously mentioned, the precrack length criterion was 0.55 to 0.6 times the fixed length to preserve stable crack growth.

References

1. Xu, S., "Evaluating Thermal and Mechanical Properties of Electrically Conductive Adhesives for Electronic Applications." Dissertation, Engineering Science and Mechanics, Virginia Tech, Blacksburg, VA, 2002.

Chapter 4: Analysis Methods

This section will cover the analysis methods chosen for each specimen geometry and test type. For the dynamic testing, crack length determination methods will be covered as well as the methods used to calculate the energy release rates. Relevant correction factors will also be discussed when applicable.

4.1: Static DCB Analysis

As previously mentioned, static DCB tests were conducted using ASTM standard D3433 on an Instron 4500 series test frame. Load and opening displacement data were collected using the built-in data acquisition system and crack length was measured using a paper ruler bonded to the side of the specimen. A corrected beam theory approach from Blackman et al. was used to analyze this data and gather mode I energy release rate values[1].

This method uses the measured load and opening displacement to calculate the energy release rate at each measured crack length[1]. The equation for the static mode I energy release rate is:

$$G_{Ic} = \frac{3P\Delta}{2B(a+\chi)}\frac{F}{N} \qquad (1)$$

where F and N are correction factors for large deflections and stiffening of the beams due to the loading end blocks, Δ is the measured opening displacement, P is the applied load, B is the specimen width, and χ is a correction factor for the compliance. A correction factor for the compliance is necessary because this method is based on simple beam theory for a perfectly cantilevered beam and thus underestimates the compliance because the beam is not perfectly built-in at the root of the crack tip.

4.2: Dynamic DCB Analysis

All dynamic DCB test data was collected using the high-speed imaging system and was outputted as an image for every moment in time recorded. National Instruments (Austin, TX) LabVIEW software was used to gather opening displacement data from these images. An edge detection code written by Brown was used to scan the images and find the x and y coordinates along each beam, as shown in Figure 4.1[5]. This code collects data every 10 pixels (~4mm) along an image and calculates the opening displacement, δ, as the difference between the y coordinates of the upper and lower beams (y_1 and y_2) at numerous points along the specimen. Half the beam thickness is subtracted from this value to give the opening displacement at each point along the sample.

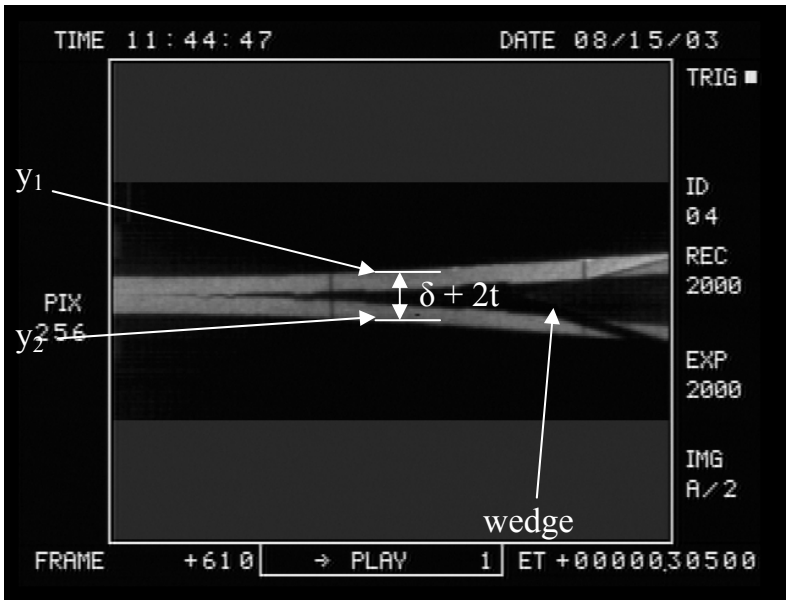

Figure 4.1. Parameters collected with edge detection program

The edge detection data for all images were then imported into an analysis program that scales the displacements from pixels to meters. A nonlinear fit was then applied to the data from each image (each instant in time) in the form of:

$$\delta = \frac{2P}{3E_f I}(-(a-x)^3 + 3a(a-x)^2)UnitStep[x-a] \qquad (2)$$

where δ is the opening displacement at a given x, P is the calculated load, E_f is the modulus of elasticity of the adherend material, I is the moment of inertia of the adherends, a is the crack length, and x is the position along the beam[5]. The crack length can then be extracted and used to calculate the energy release rate using an equation developed by Blackman et al.[2]:

$$G_I = \frac{9\Delta^2 E_f I}{4Ba^4} F \tag{3}$$

where Δ is the opening displacement at the load application point, B is the specimen width, and F is a correction factor for large deflection.

This analysis method was successfully used by Brown, and as a result very few issues had to be resolved to obtain acceptable results for the chosen adhesive/composite system. The unstable crack growth encountered with the chosen system created problems with the analysis resolution, specifically with the nonlinear fit used to determine the crack length. This analysis resolution, if set too high, led to extremely long analysis times, however, if set too low, test data was not properly fitted, leading to incorrect crack length predictions. Issues were also encountered with 36 ply and aluminum adherend specimens as less deflection was required for crack propagation, resulting in less data per test run, as well as more sensitivity to noise in the test data. This increased debonding rate as a result of the relative stiffness of the aluminum and 36 ply adherends exceeded the capability of the imaging system in some cases, resulting in lost data, specifically at crack initiation. This issue could be resolved by using an imaging system with a higher sampling rate.

4.3: Dynamic ELS Analysis

End-loaded split data was collected using the high-speed imaging system and was imported into an analysis program and scaled in the same fashion as the Dynamic DCB data. The analysis method for the ELS geometry was developed with the help of Johnson, and involves using a least squares fit between two equations based on beam theory that describe both the cracked and uncracked portions of the beam. This least-squares method was used because the crack length cannot be determined visually since the beams travel in the same direction as the specimen is deflected. A sample of this crack length determination code is shown in Appendix D.

The least-squares method involves fitting cubic equations to both the cracked and uncracked portions of the ELS beam by using boundary and transition conditions to determine the coefficients of the equations.

$$w_1 = b_3 x^3 + b_2 x^2 + b_1 x + b_0 \tag{4}$$

$$w_2 = c_3 x^3 + c_2 x^2 + c_1 x + c_0, \tag{5}$$

where w_1 and w_2 are the deflections of the uncracked and cracked portion of the beam, respectively, and x is the position along the beam. The coefficients are defined as shown in Figure 4.2.

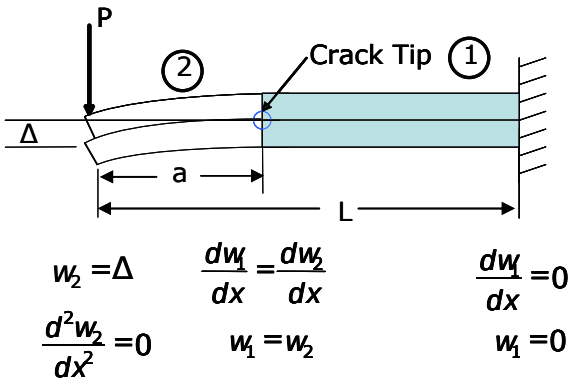

Figure 4.2. ELS geometry boundary and transition conditions

Once the crack length is determined, the energy release rate can be calculated using an equation developed by Blackman et al.[3]:

$$G_{II} = \frac{9\Delta^2 h^3 E_f (a + \chi_{11} h)^2}{[3(a + \chi_{11} h)^3 + (L + 2\chi_1 h)^3]^2} \frac{F}{N^2} \tag{6}$$

where Δ is the opening displacement, h is the beam thickness of the adherends, a is the crack length, E_f is the modulus of elasticity of the adhesive, L is the fixed length of the specimen, χ_I and χ_{II} are correction factors for deflection and end-rotation of the crack tip, and F and N are correction factors for large deflections and stiffening of the beams due to the loading end blocks.

A sensitivity study was conducted on this analysis method to determine the effect of noise in the images collected during testing. An ideal data set based on a beam theory prediction was created with a specimen length of 200 mm and a predetermined crack length of 125 mm. Random noise of ±0.01, ±0.1, ±0.5, and ±1 mm was then added to the deflection values in the ideal data set to determine the effect of each noise level on the crack length prediction. The results of the analysis showed an average of 10% error in the crack length prediction when ±1 mm of noise was added to the deflection values, and a fraction of a percent error for all other noise levels. The average maximum deflection in the testing was approximately 68 mm, thus 1 mm of noise creates an overall error of approximately 1.5% in relation to the maximum deflection. The likely data collection error is approximately 1 pixel, which roughly equates to 0.5 mm, resulting in 0.75% error due to noise in the collected test data.

Because the ELS analysis method was newly developed, many issues were encountered in determining the crack length. Initial testing was conducted with 36 ply composite adherends and it was discovered that because of the stiffness of the adherends,

there was not enough deflection for the least squares fit to determine the crack length. As a result, 12 ply specimens were tested as the decreased stiffness produced much larger deflections. Problems with crack prediction were still encountered due to small scaling errors and noise in the test data due to light placement. It was found that conversion factors and length measurements had to be carefully measured for each test run, as small differences substantially changed crack length predictions. Also, the angle of the lighting used to illuminate the substrates for edge detection was found to be crucial in reducing noise in the test data. Camera placement and zoom were also important, especially in the case of the 12 ply adherends. Due to the large deflections, the image window had to be optimized such that the adherends did not travel out of the viewable range, causing a loss of data.

The unstable crack growth also produced unclear results within the analysis program, as crack predictions leading up to the point of propagation were erratic because there was no crack growth until that point. As a result, the image prior to propagation had to be identified such that only the crack length at that point was utilized in the analysis. The unstable growth did, however, provide a solid means for verifying results obtained from the analysis program as the crack length prior to initiation was clearly identifiable due to the arrest lines in the adhesive layer. Once camera and light placement as well as scaling issues were resolved, crack length predictions from the analysis program matched physical measurements on test specimens within 1%.

4.4: Dynamic SLB Analysis

The crack length for the single leg bend geometry was determined in a similar fashion to that of the end-loaded split geometry. Cubic equations were developed for

both the cracked and uncracked portions of the beam and coefficients were determined using the boundary and transition conditions shown in Figure 4.3. A sample of the crack length determination code for this geometry is shown in Appendix D.

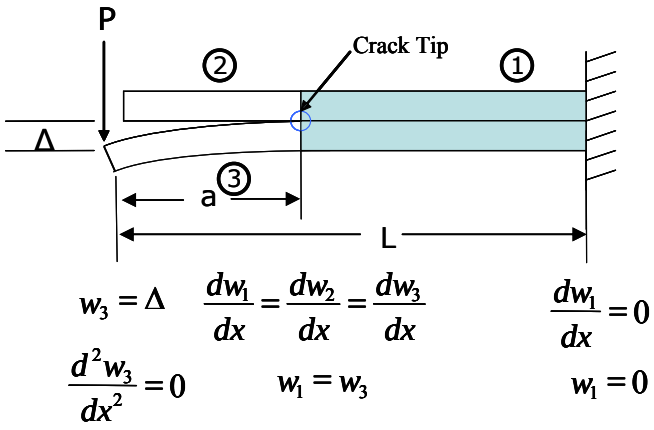

Figure 4.3. SLB geometry boundary and transition conditions

Once the crack length was determined, the mixed-mode energy release rates were calculated using equations developed by Blackman et al.[3]:

$$G_I = \frac{12\Delta^2 h^3 E(a+\chi_1 h)^2}{[7(a+\chi_{11}h)^3 + (L+2\chi_1 h)^3]^2} \frac{F}{N^2} \tag{7}$$

$$G_{II} = \frac{9\Delta^2 h^3 E(a+\chi_{11} h)^2}{[7(a+\chi_{11}h)^3 + (L+2\chi_1 h)^3]^2} \frac{F}{N^2} \tag{8}$$

where all parameters are as previously defined.

A sensitivity study was also conducted on this analysis method. As in the case of the ELS sensitivity analysis, random noise of ±0.01, ±0.1, ±0.5, and ±1 mm was added to the deflection values in the ideal data set to determine the effect of each noise level on the crack length prediction. The results of the SLB sensitivity analysis showed an average of 10% error in the crack length prediction when ±1 mm of noise was added to the deflection values and fractional errors for the lesser values, as in the case of the ELS

analysis. The average maximum deflection in the testing was approximately 33 mm, thus 1 mm of noise creates an overall error of approximately 3% in relation to the maximum deflection. The likely data collection error is approximately 1 pixel, which roughly equates to 0.5 mm, resulting in 1.5% error due to noise in the collected test data.

Similar issues with camera and light placement were encountered with the SLB testing as well. The same precautions were taken as in the case of the ELS testing to ensure correct crack length prediction. Because only one beam was deflected by the loading tup in this case, image window optimization was crucial to prevent the loss of test data. The SLB geometry was, however, less sensitive to scaling because the beams were separating as a result of the combined loading mode, as opposed to the ELS geometry where they were traveling in unison.

References

1. Blackman, B.R.K., Kinloch, A.J., "Fracture Tests for Structural Adhesive Joints," *Fracture Mechanics Testing Methods for Polymers, Adhesives and Composites*, Amsterdam: Elsevier Science, 2001.
2. Blackman, B.R.K., Dear, J.P., Kinloch, A.J., Macgillivray, H., Wang, Y., Williams, J.G., Yayla, P., "The failure of fibre composites and adhesively bonded fibre composites under high rates of test. Part I: Mode I loading-experimental studies," *Journal of Materials Science*, **30** (1995), 5885-5900.
3. Blackman, B.R.K., Dear, J.P., Kinloch, A.J., Macgillivray, H., Wang, Y., Williams, J.G., Yayla, P., "The failure of fibre composites and adhesively bonded fibre composites under high rates of test. Part III: mixed-mode I/II and mode II loadings," *Journal of Materials Science*, **31** (1996), 4467-4477.
4. Brown, S., "Time and temperature-dependence of fracture energies of copper/epoxy bonds." Thesis, Engineering Science and Mechanics, Virginia Tech, Blacksburg, VA, 2004.
5. Wolfram Research. (2003). *Mathematica 5.0.* IL: Wolfram Research, Inc.

Chapter 5: Results and Discussion

This section will cover the test results collected in modes I and II as well as DSC data collected on the adhesive cure cycle. As previously mentioned, static and dynamic DCB tests were run using both aluminum and composite adherends and dynamic ELS and preliminary SLB tests were run using composite adherends. Static DCB results will be covered first including cure study and relative stiffness analysis results, followed by dynamic DCB, ELS, and SLB results.

5.1: Static DCB

Testing on this project began with static DCB experiments on aluminum adherends. Initial testing resulted in very few data points per specimen due to unstable crack growth within the adhesive layer. Specimens were loaded until the point of crack initiation, at which time the crack would rapidly grow 40-60mm before arresting. Issues with specimen quality resulting from inconsistent curing were also discovered. In an attempt to reduce the crack jump distance, the bondline thickness was changed from 0.8 mm to 0.5 mm. The curing process was also more closely monitored to ensure consistent curing. After these changes, three to four data points were collected on each test specimen. It is unclear which change resulted in the increase in data points, the reduction in bond thickness was an attempt to restrict the plastic zone size and possibly the crack jump distance, but as later calculations show, it is unclear whether the plastic zone is being restricted by the 0.5 mm bondline. The results of the static DCB testing using the 0.5 mm bondline are shown in Figure 5.1.

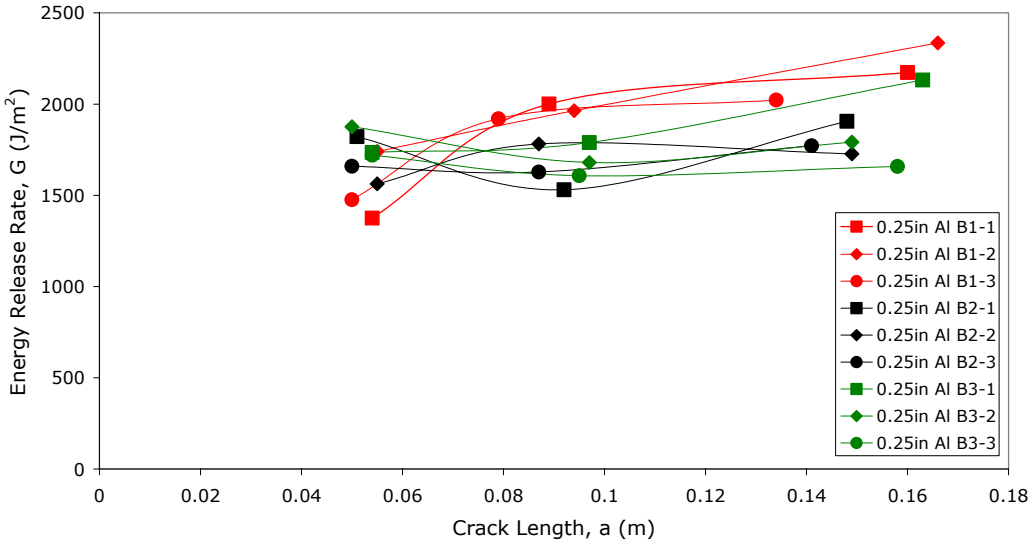

Figure 5.1. Initiation SERR, static DCB on aluminum with 1 mm/min test rate

Figure 5.1 shows the initiation energy release rates for three batches of aluminum DCB specimens, with an average of approximately 1800 J/m^2 and a standard deviation of approximately 110 J/m^2. These values were calculated by inputting load, crack length, and opening displacement values prior to crack initiation into the corrected beam theory equations previously presented. The lines shown in the figure are simply to guide the eye by connecting data points within a single test. Due to previous issues with batch-to-batch variation between test samples, three batches were tested to ensure that the final method chosen for specimen preparation reduced the variation in results. The data from these tests is sufficiently more consistent than previously collected results on samples with large bondline and cure temperature variations, leading to the conclusion that the current preparation methods are satisfactory.

The arrest values for the static DCB tests with aluminum adherends are shown in Figure 5.2. These values were calculated by inputting load, crack length, and opening displacement values collected following crack arrest into the corrected beam theory equations previously presented.

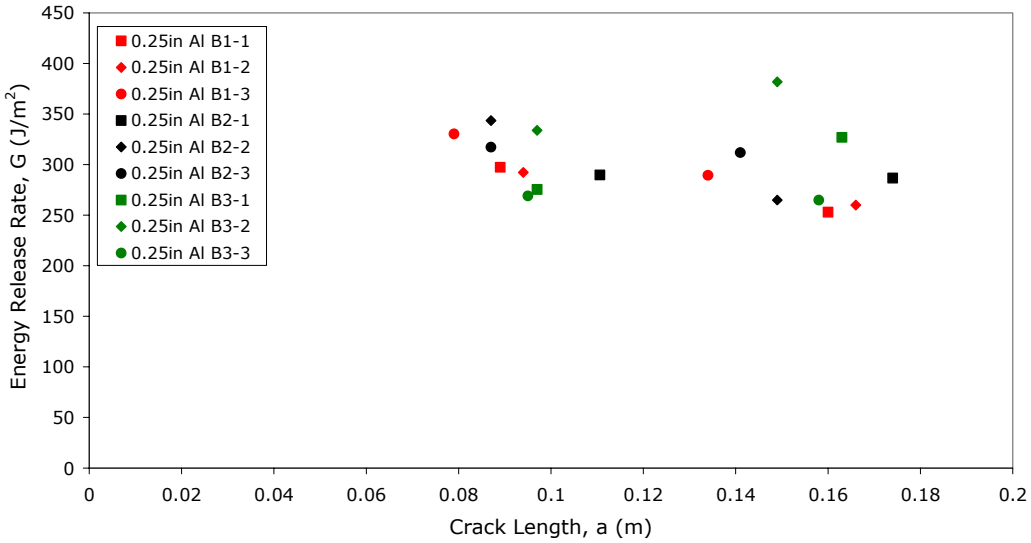

Figure 5.2. Arrest SERR, static DCB on aluminum with 1 mm/min test rate

The most notable aspect of these arrest results is the fact that the arrest values are only approximately 17% of the initiation values as a result of the unstable crack growth. These low values are most likely an artifact of the time dependent behavior of the chosen adhesive and might possibly also be due to some kinetic energy effects as a result of the rapid crack growth. Crack jump distances of up to 150 mm were observed in static DCB testing, which is comparable to stick-slip results collected by Blackman et al. who show jumps of up to 100 mm[1].

This effect of the unstable propagation can be seen in the load versus opening displacement traces collected during testing as well. Once such trace is shown in Figure 5.3. As the figure shows, as much of a 65% drop in load was experienced upon crack propagation due to up to 60 mm of rapid growth upon initiation.

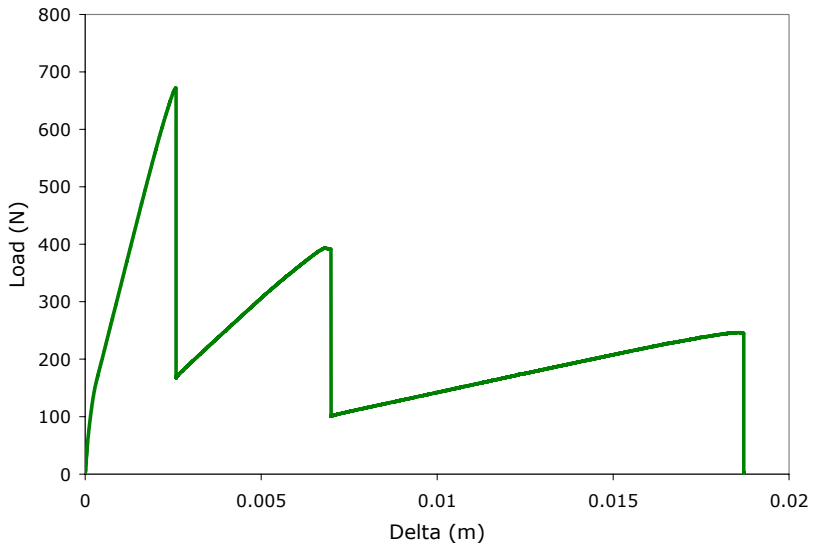

Figure 5.3. Load versus time trace, static DCB on aluminum with 1 mm/min test rate

Because of the dynamic effects resulting from the rapid propagation, the arrest values were considered to be less significant, however, the initiation energy release rates were insufficient to fully characterize the behavior of the chosen adhesive. As a result, an average critical energy release rate based on energy methods was developed to better describe the energy absorbed during rapid crack propagation. Figure 5.4 shows the load versus opening displacement data from the first propagation event for the test shown in Figure 5.3. Using the energies depicted by regions 1 and 2 in Figure 5.4, which assumes rapid crack growth occurs at a fixed displacement, an energy balance can be characterized by the equation:

$$U_2 - U_1 = G_c(\mathring{a}) * \Delta A + T_{residual} + dissipated\ \ energy \qquad (1)$$

where U_1 and U_2 represent the stored energy at locations 1 and 2 respectively, $G_c(\mathring{a})$ is the rate dependent critical energy release rate, ΔA is the area difference, $T_{residual}$ is the residual kinetic energy, and the dissipated energy may include energy going into noise

and heating the surrounding air. This equation can then be expressed in the form of an inequality for the average energy release rate:

$$G_{c_{ave}} \leq \frac{U_2 - U_1}{A_2 - A_1} \tag{2}$$

where A_1 and A_2 are the bond areas corresponding to the initial and final crack, and the inequality takes into account the ignored kinetic energy, noise, and other effects. For the example shown, the average energy release rate was determined to be approximately 400 J/m^2, much lower than the peak value of 1720 J/m^2, but above the arrest value of 270 J/m^2.

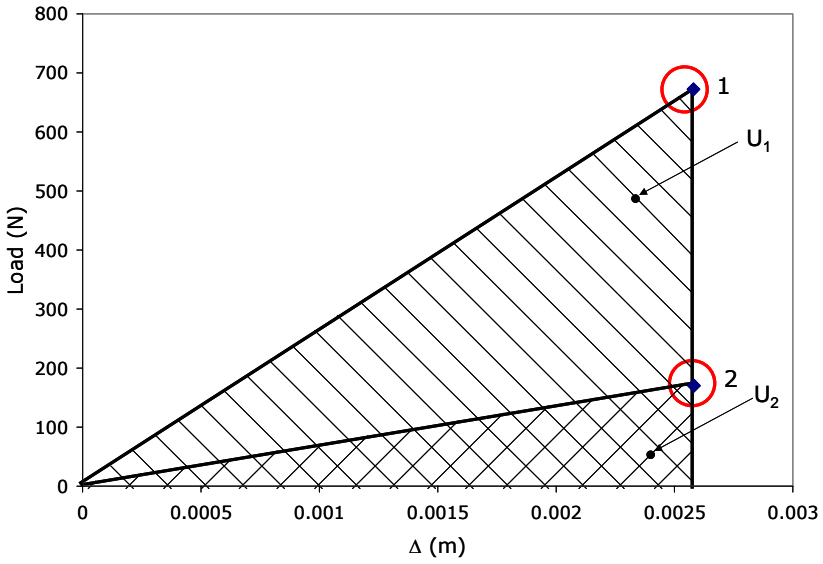

Figure 5.4. Load versus time trace, load drop after first initiation

Static DCB tests were also conducted using the supplied composite adherends in 11 and 36 ply configurations, which are 2.5 mm and 8.5 mm thick, respectively. Initially, precracks immediately grew into the composite adherends rather than growing within the adhesive layer. Results from these tests, which indicate the interlaminar energy release rate of the composite material, are shown in Figure 5.5. The average energy release rate

of the composite material was approximately 550 J/m^2, 1250 J/m^2 lower than the initiation energy release rate of the adhesive measured using the aluminum adherends.

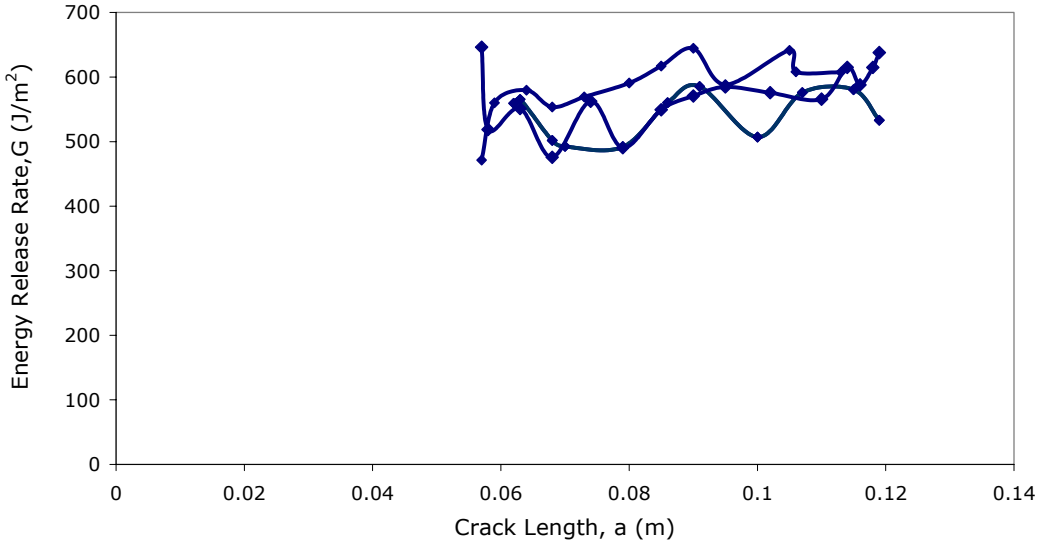

Figure 5.5. Results for interlaminar crack growth within composite adherends

5.1.1: Static DCB with New Precracking Technique

After trying multiple techniques to keep the crack growth within the adhesive layer, heating composite specimens prior to precracking was found to induce crack growth within the adhesive material. The final preheating procedure entails placing specimens in an oven set at 200°C for ten minutes and then immediately precracking them at an elevated temperature as detailed in the specimen preparation section of this thesis.

No explanation has been found as to why this preheating procedure works. Possibly, the heating of the adhesive above its T_g during the preheating, makes it softer and more fluid-like, thus reducing the fracture energy necessary to propagate the crack within the adhesive layer. This may also cause further curing of the adhesive, thus

lowering the fracture toughness, which may explain why crack propagation remains in the adhesive layer during testing at room temperature.

Results for static DCB tests on 12 ply and 36 ply composite using the heated precrack procedure are shown in Figure 5.6. 36 ply specimens were made with a 0.5 mm bondline thickness, and 12 ply composite specimens were made with both 0.5 mm and 1 mm bondline thicknesses to investigate the effect of the bondline thickness on the fracture energy. Based on preliminary bulk tension (dogbone) and compact tension testing, the plastic zone radius is 0.26 mm, which could indicate that the plastic zone is being restricted by the bondline in the case of the 0.5 mm bondline thickness. No significant difference was found between the 1 mm and 0.5 mm bondline thickness specimens, leading to the conclusion that the 0.5 mm thickness is not significantly constricting the plastic zone. Two batches of each bondline thickness were tested for both adherend thicknesses, again looking at the batch to batch variations. Unstable crack growth is evident as in the case of the aluminum adherend specimens, resulting in rapid crack propagation and very few data points per specimen.

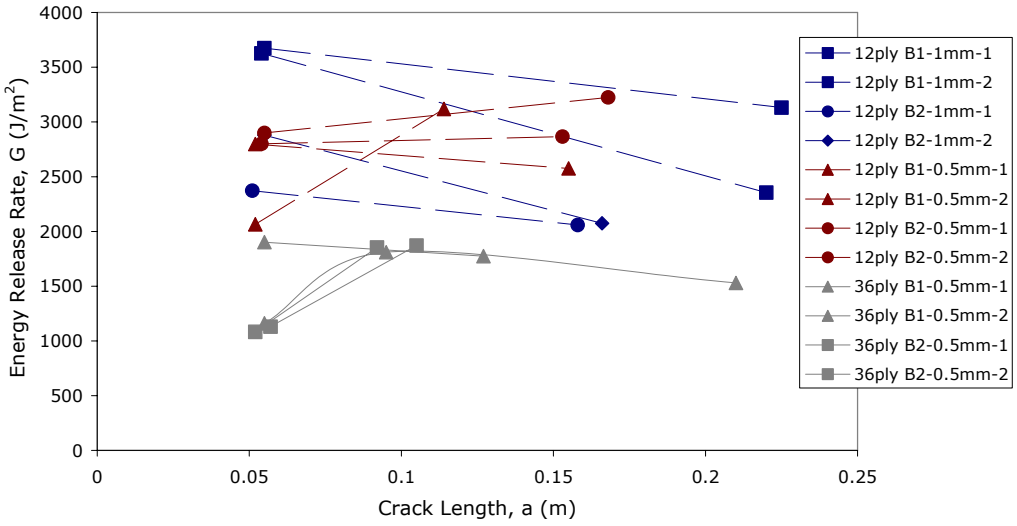

Figure 5.6. Static DCB initiation energy release rates, 12 and 36 ply composite

Initiation energy release rates averaged 2700 J/m^2 for the 12 ply composite specimens and 1600 J/m^2 for the 36 ply composite specimens. These values are as much as 2150 J/m^2 greater than that of the composite material, yet the crack propagation remains in the adhesive layer regardless of the fact that the composite is actually the "weakest link"[2].

The 12 ply specimens exhibited higher initiation energy release rates as well as longer crack jumps between propagation points. Several theories were developed to explain this behavior. The first suggested that this behavior is a result of the difference in stiffness between the two thicknesses of composite adherends. The stiffness of each adherend type and thickness were calculated, and the results of this study are shown in Table 5.1.

Table 5.1. Stiffness of aluminum and 12 and 36 ply composite adherends

Material	Stiffness (N*m)
Aluminum	38
12 ply composite	2
36 ply composite	50

As Table 5.1 shows, the 12 ply adherends are significantly less stiff than the 36 ply and aluminum adherends, leading to the conclusion that the stiffness differences could in fact be causing the variation in test results. Evidence in the literature was found that supported this claim, showing that stiffer adherends led to a higher local loading rate at the crack tip, even when specimens were loaded at the same rate globally[3]. This lower local loading rate in the thinner, less stiff, adherends leads to a larger and more defined plastic zone, thus requiring a higher amount of energy to initiate the crack. The plastic zone size for both the 12 and 36 ply adherends was calculated as 0.42 mm and 0.25 mm respectively, using the Dugdale method, further showing that that the 12 ply adherends

are being loaded slower locally, leading to a larger plastic zone as well as a higher energy release rate[4].

Another theory was developed to explain the difference in the 12 and 36 ply specimen results which suggested additional curing in the 36 ply specimens due to heat being held longer in these specimens during the curing process. If true, additional curing is possible, making the thicker adherend specimens more brittle, thus leading to lower initiation energy release rates. This was due to the fact that the adhesive was not being fully cured initially, as recommended by the supplier. The first step in determining if the amount of cure was a factor was to monitor the bondline temperature of the bonded panels during the curing process. An Omega Engineering (Stamford, CT) Type J thermocouple was placed at the center of a 12 and a 36 ply panel during the curing process and the temperature was recorded over the span of the adhesive cure. These temperature measurements are shown in Figure 5.7.

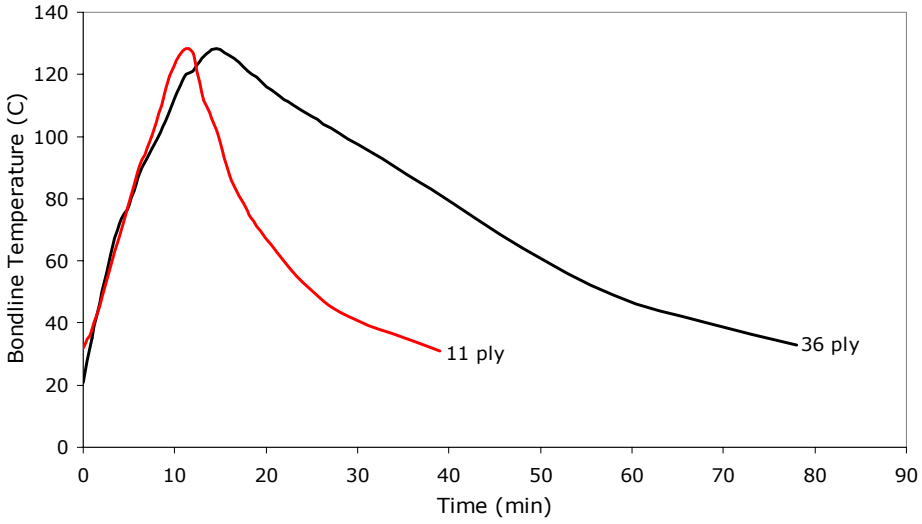

Figure 5.7. 12 and 36 ply specimen temperature profiles during curing

As Figure 5.7 shows, heat is held within the 36 ply specimens longer during the curing process, possibly leading to additional curing.

The next step was to conduct a cure study using a TA Instruments DSC 2920 differential scanning calorimeter (New Castle, DE) to determine the degree of cure in the bulk adhesive after different periods of curing time. A 5 mg sample of uncured epoxy was placed in the DSC and heated in air to the cure temperature (120°C) at a rate of 20°C/min. The temperature was then held for 10 minutes to examine the dynamics of the curing process. The DSC trace from this testing is shown in Figure 5.8. The curved trace represents the heat flow with the exothermic direction up, and the sloped line is the temperature trace.

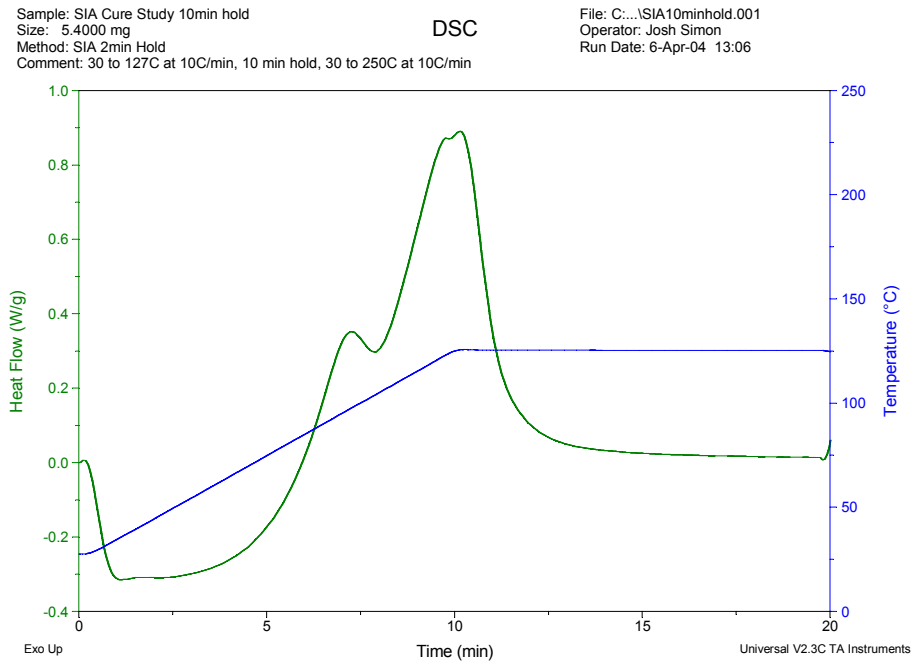

Figure 5.8. DSC trace for 10 minute hold at cure temperature

To determine the degree of cure, the heat flow versus time trace was integrated using the TA Instruments Thermal Analysis software to get the area under the curve. The degree of cure was then calculated using the equation:

$$\%Cured = \frac{A_{Current}}{A_{total}} \qquad (3)$$

where $A_{current}$ is the area under the heat flow curve up to the point in time of interest and A_{total} is the total area under the heat flow curve from the onset of curing to the point where the adhesive is fully cured. A plot of the degree of cure versus time is shown in Figure 5.9 along with the temperature trace.

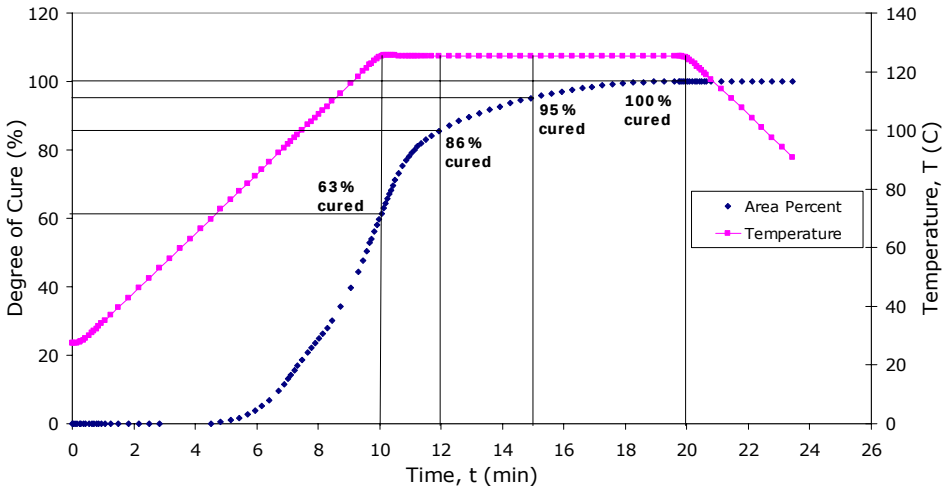

Figure 5.9. SIA adhesive degree of cure

As Figure 5.9 shows, significant curing occurs in the first five minutes at the cure temperature (127°C), and a large variation in cure is possible in the 2-5 minute range suggested by the manufacturer. As a result, it was decided to fully cure the adhesive in both the aluminum and composite specimens by keeping them at the cure temperature of 127°C for 5 minutes during the curing process.

5.1.2: Bondline Thickness Study

The bondline thickness variation of a sample of specimens from each batch was analyzed to determine potential problems. Measurements were taken every 25 mm along the specimen from 25 to 250 mm. These results were then analyzed for each adherend type and bondline thickness. Figure 5.10 shows the results for aluminum specimens with

a 0.5mm bondline, Figures 5.11 and 5.12 show results for 12 ply composite specimens with a 1mm and 0.5 mm bondline thickness, respectively, and Figure 5.13 shows results for 36 ply composite specimens with a 0.5mm bondline thickness.

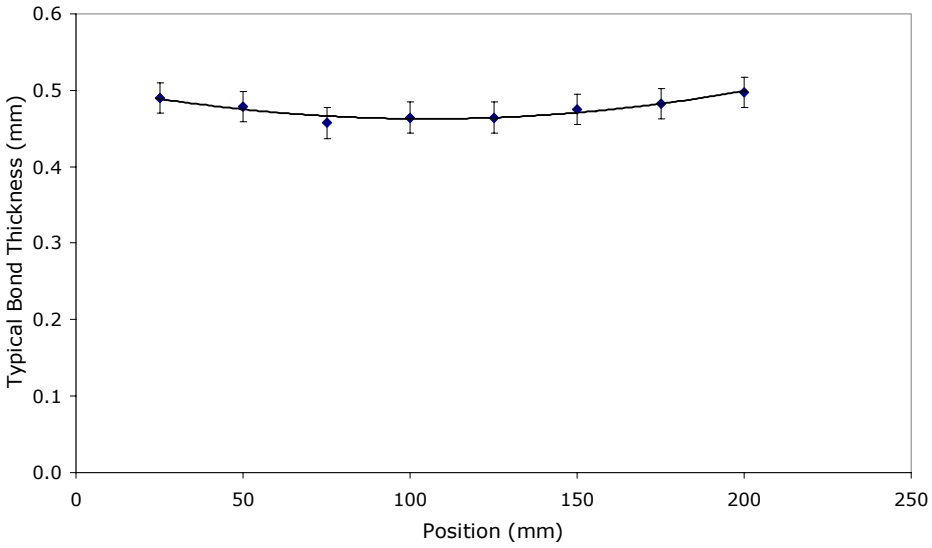

Figure 5.10. Bondline thickness variation—6.35 mm aluminum with 0.5 mm bondline

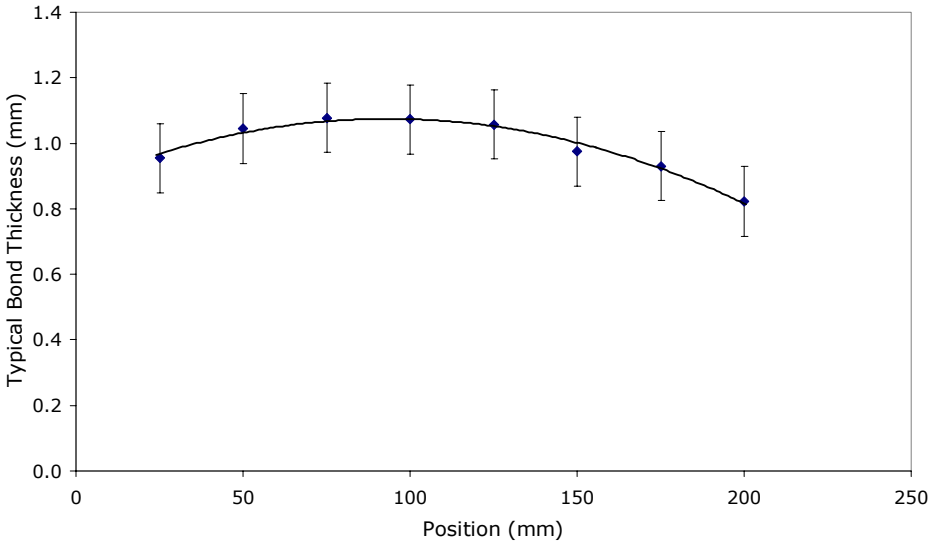

Figure 5.11. Bondline thickness variation—12 ply composite with 1 mm bondline

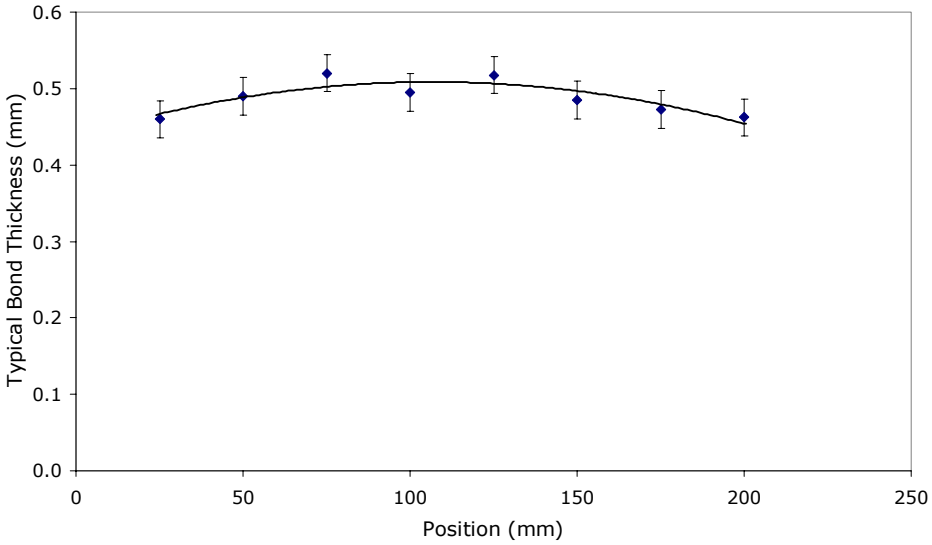

Figure 5.12. Bondline thickness variation—12 ply composite with 0.5 mm bondline

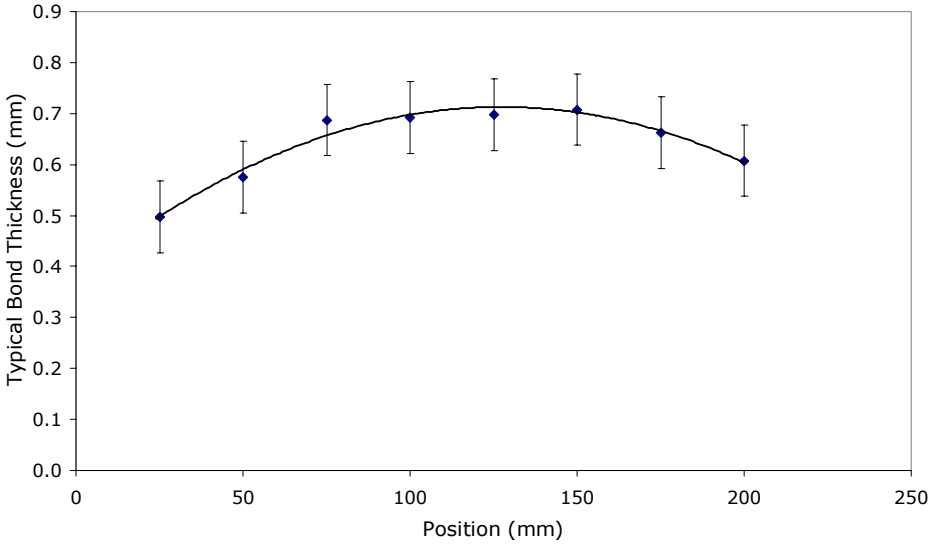

Figure 5.13. Bondline thickness variation—36 ply composite with 0.5 mm bondline

More variation is seen with the aluminum specimens, most likely because these specimens are clamped with binder clips rather than being bonded using the platen press. The variations in each case are less than 10% and are acceptable for this type of specimen.

5.1.3: Static DCB with C-clamp and 400 mm Specimens

Due to the lack of obtainable data as a result of the unstable crack growth, a C-clamp technique was implemented in an attempt to gather multiple initiation points per test specimen. Specimens were prepared in the same fashion as before, but a C-clamp was placed 25mm from the crack tip after each initiation to stop the crack after propagation. This method only produced initiation values, but due to the previously mentioned dynamic effects, arrest values were determined to be less meaningful for the system being studied. The results from these C-clamp tests are shown in Figure 5.14. These tests provided 7-8 data points for 11 ply specimens and 3-4 for 36 ply specimens. The C-clamp had to be placed farther from the crack tip for the 36 ply specimens due to the stiffness of the adherends, and as a result, fewer data points were gathered than on the 11 ply specimens.

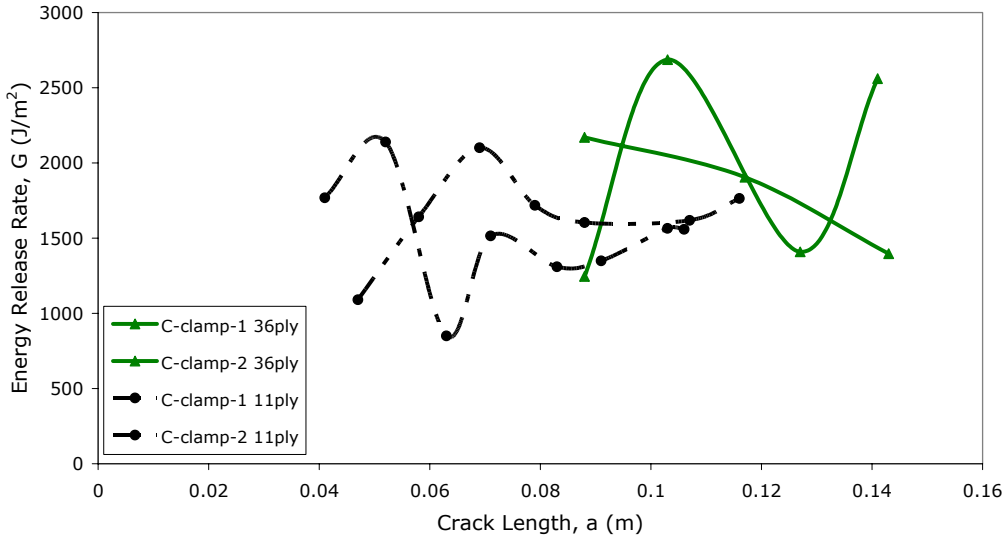

Figure 5.14. Static DCB with C-clamp on 11 and 36 ply composite

Longer DCB specimens were also constructed out of 11 ply composite. The goal of using these longer specimens was to gather more than two initiation and arrest points per test. These specimens were bonded in the same fashion as the standard length

specimens, but were cut in 400 mm lengths. Initial testing revealed that only three data points could be collected from each specimen, one more than the standard length specimens, because after the second initiation, the crack grew over 200 mm. Also, the duration of the test runs was more than doubled by using the 400 mm specimens. As a result, the testing of the 400 mm static DCB specimens was aborted in the interest of time.

5.2: Dynamic DCB

Dynamic DCB tests were also conducted on both aluminum and composite adherends using the aforementioned drop tower. The results from the tests on aluminum are shown in Figure 5.15 and those on composite are shown in Figure 5.16. These figures show the apparent energy release rate, sampled at 2000 frames/second and not necessarily the discrete initiation and arrest energy release rates. This apparent energy release rate is the applied energy release rate, not a critical value, over the duration of the test and possibly includes dynamic effects due to the test rate.

In the case of these dynamic tests, the unstable crack growth created problems in capturing the critical energy release rates as well as in providing sufficient data to calculate crack velocities. Because of the rapid crack propagation, data was lost as the crack velocity exceeded that which the available imaging system was capable of recording. A system with a higher sampling rate could capture more data leading up to initiation, possibly resulting in higher calculated critical energy release rates as well as more complete crack velocity data, showing definite initiation and arrest points.

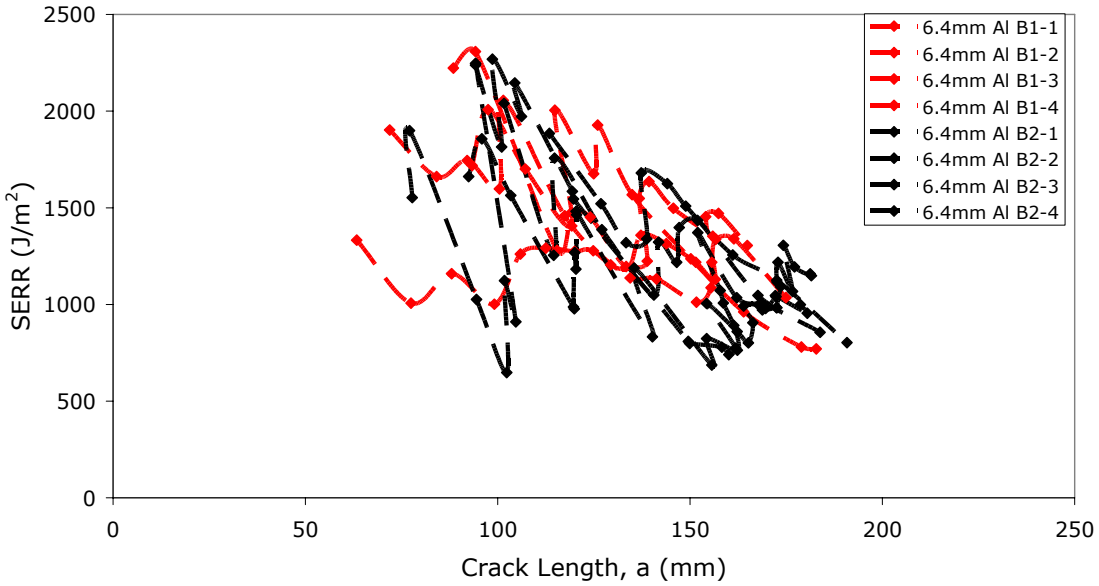

Figure 5.15. Dynamic DCB with 6.35 mm aluminum adherends

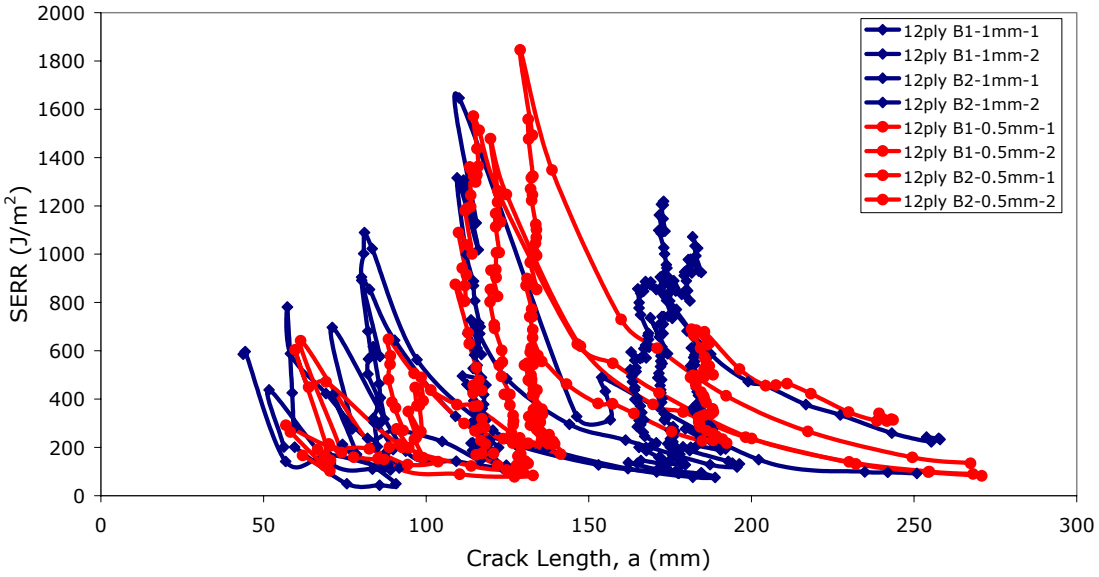

Figure 5.16. Dynamic DCB with 12 ply composite adherends

Because of the number of data points collected per test, the sampled results are difficult to interpret when plotted together. One significant difference between the aluminum and composite results is the fact that there are peaks and valleys in the

composite data, whereas the aluminum results are fairly constant. This disparity is most likely an indication of stick-slip crack growth in the case of the 12 ply composite due its lower relative stiffness. Also, there is an apparent convergence in energy release rate values in Figure 5.15 as the crack length increases. This is possibly due to lost data as a result of an insufficient sampling rate. This hypothesis could be verified by using a camera with a higher sampling rate and comparing the results to those shown in Figure 5.15.

Because of the flexibility of the 12 ply composite adherends, the local loading rate is reduced enough to allow plastic zones to form ahead of the crack tip, causing unstable growth, even at this high global loading rate. Figure 5.17 shows the crack velocity versus time and energy release rate versus time for a single test for the 12 ply composite adherends.

The velocity data indicates two possible arrest points for the 12 ply test, corresponding to peaks in the energy release rate data. Because the velocities are calculated using a finite difference and are not instantaneous, strong claims cannot be made about crack arrests based on the information shown in the figures. With a higher speed camera and a method to obtain instantaneous velocity data, it would be possible to determine if there are in fact crack arrests during dynamic DCB tests. The results shown do indicate that the crack velocity is changing and peaks in energy release rate correspond to valleys in the crack velocity as expected.

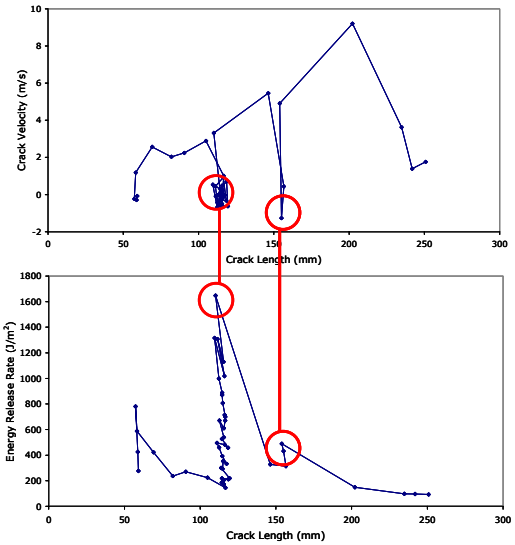

Figure 5.17. Dynamic DCB with 12 ply composite adherends, crack velocity and energy release rate versus time from a single test

To provide a means for comparison of the dynamic data to static DCB results, Figure 5.18 shows only the peaks of the 12 ply composite dynamic DCB results, which may or may not represent the actual critical energy release rates. The peaks in energy release rate may or may not have been captured because the data collection was limited to 2000 frames/second by the imaging system. These results could be verified by using a higher speed imaging system to capture more data points per test.

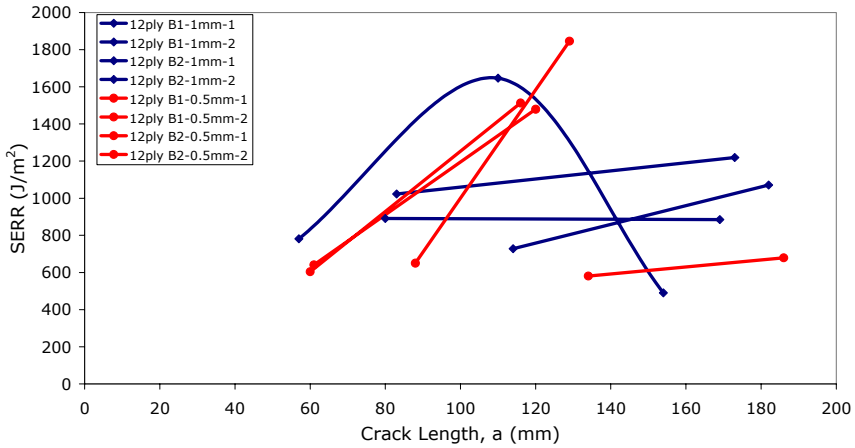

Figure 5.18. Peak energy release rates—12 ply dynamic DCB

The average "peak" energy release rate for these dynamic tests is 1000 J/m^2, which is significantly lower than the static initiation energy release rate of 2700 J/m^2. This reduction in energy release rate may be due to the sampling rate of the imaging system, but could also be due to a smaller plastic zone being formed at the crack tip as a result of the higher loading rate, both globally and locally. Approximate plastic zone size for the static DCB was 0.42 mm, whereas the dynamic DCB plastic zone size was 0.16 mm. These values were calculated using the previously mentioned Dugdale method with the yield stress value of 55 MPa deduced from bulk tensile testing and the stress intensity factors calculated using the average measured static and dynamic DCB energy release rates.

5.3: Loading Rate Effects

Significant differences were found between the fracture surfaces of static and dynamic DCB specimens at suspected arrest sites. This was expected due to similar findings in the literature reviewed as well as because of the plastic zone size calculations done for the purposes of this thesis. A scanning electron microscope (SEM) was used to examine the fracture surfaces of these specimens at a single arrest site. The results from these scans are shown in Figures 5.19 and 5.20. As was expected, the suspected arrest sites on the static test surfaces were significantly rougher, with larger and more defined plastic zones.

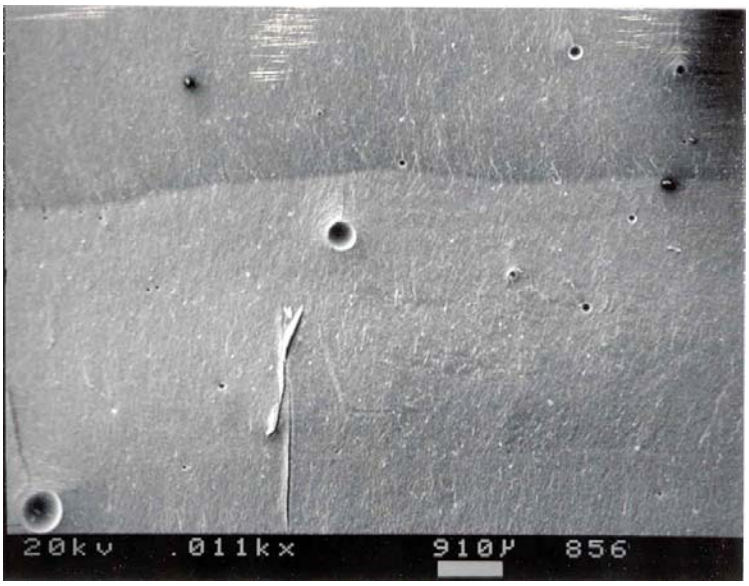

Figure 5.19. Dynamic DCB fracture surface at suspected arrest site

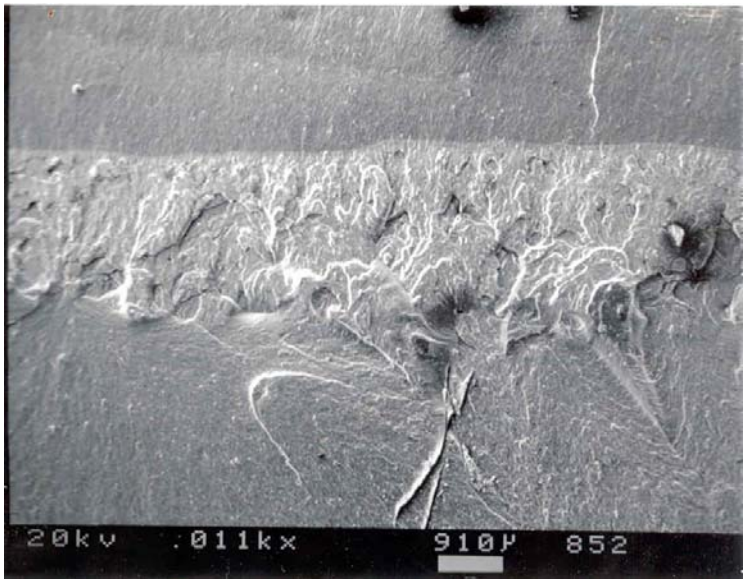

Figure 5.20. Static DCB fracture surface at suspected arrest site

The effect of the global loading rate on both the test results and the fracture surfaces is very distinct. Several methods were attempted to demonstrate the effects of the local loading rate on the test results as well. The best illustration found to show this artifact of the relative stiffness differences between adherends is shown in Figure 5.21. The curve with the upward trend shows the initiation energy release rate for a 12 ply

composite specimen that was C-clamped 25 mm from the crack tip after each initiation point, in the same manner as the previously reported C-clamp tests. The curve with the downward trend depicts the applied G_{dot} at failure for each crack initiation. These results clearly show a rise in energy release rate as the crack travels farther along the specimen, effectively lengthening the beams and lowering the local loading rate. This phenomenon of increasing energy release rate was not found in all test results, but this experiment does depict the effect of the local loading rate on the critical energy release rate.

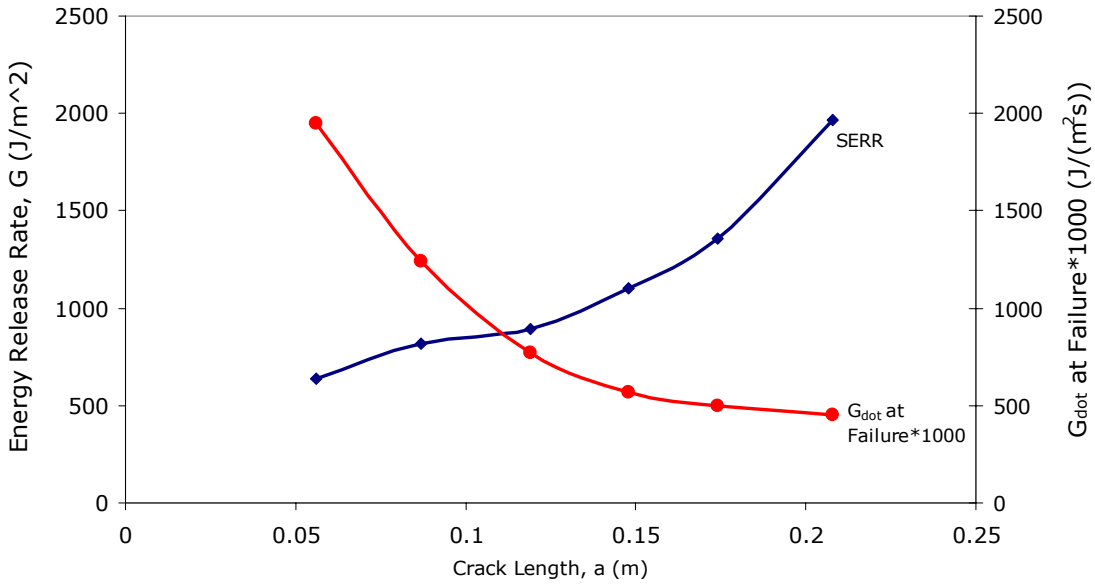

Figure 5.21. 12 ply static DCB with C-clamp—local loading rate effect

5.4: Mode II and Mixed Mode I/II

Dynamic ELS testing was also conducted to obtain mode II energy release rates. These tests were run using the drop tower configured as described in the test setup section of this thesis. Figure 5.22 shows the results from the dynamic ELS testing for both 1 mm and 0.5 mm bondline thicknesses calculated using the aforementioned

analysis program. These results were verified by hand using estimated displacement and crack length measurements made with the LabVIEW Vision software. The results obtained from the analysis program were found to be within 10% of the results calculated by hand. As the figure shows, only one data point was collected per specimen because the crack traveled into the composite material after propagating from the precrack in the adhesive layer. The average initiation energy release rate for the 0.5 mm bondline thickness was 3100 J/m^2 and the average value for the 1 mm bondline thickness was 750 J/m^2.

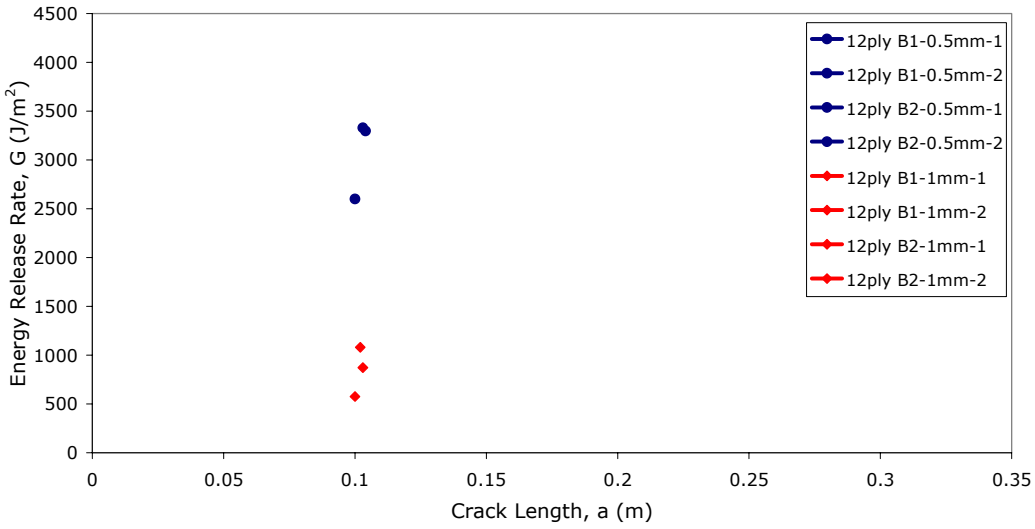

Figure 5.22. 12 ply dynamic ELS with 0.5 and 1 mm bondline thicknesses

The fracture surfaces of the 1 mm thickness specimens were very non-uniform, as was the precrack, possibly leading to the low average energy release rate. There were also possible issues with the curing of the 1 mm specimens, but due to time constraints more specimens could not be made. Figure 5.23 shows the differences in the fracture surfaces between the 0.5 mm and 1 mm bondline thickness specimens.

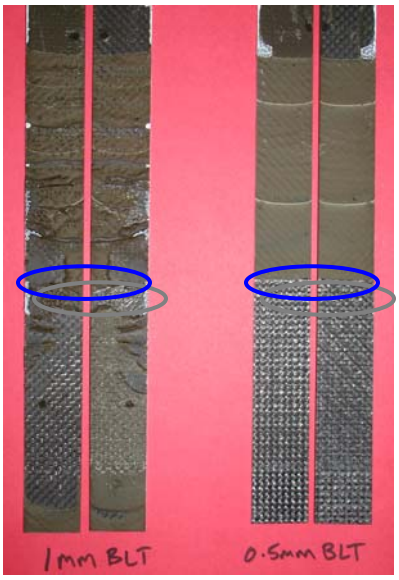

Figure 5.23. 12 ply dynamic ELS fracture surfaces, 1 mm and 0.5 mm bondlines

As Figure 5.23 shows, the 1 mm bondline thickness specimen has a very non-uniform fracture surface whereas the fracture surface of the 0.5 mm bondline thickness specimen is fairly smooth and uniform. The precrack region, noted by the circle in the image, is also very non-uniform in the case of the 1 mm bondline thickness specimen. Because the only data point collected from these tests is an initiation from this precrack, the data may be suspect due to the non-uniformity of the precrack.

5.4.1: Mixed Mode I/II

Preliminary dynamic SLB testing was also conducted to obtain mixed-mode data. These tests were run with symmetric specimens, which produced a mode I to mode II ratio of 1.33. This testing resulted in energy release rates on the order of 1000 J/m^2 for mode I and 1400 J/m^2 for mode II. These values, calculated using the developed analysis program, were verified to be within 10% of values calculated by hand, as in the case of the ELS results. This agreement in results led to the conclusion that the analysis program

was sufficiently predicting the crack length. Further testing will be conducted on this geometry, but will not be included in this thesis due to time constraints.

5.5: Conclusion

Static and dynamic DCB tests were run with 6.35 mm aluminum and 12 ply adherends, and 36 ply composite adherends were also tested statically. Dynamic ELS and SLB tests were also run with 12 ply composite adherends. Table 5.2 shows the initiation energy release rates for the static DCB and dynamic ELS and SLB testing, the peak energy release rates from dynamic DCB testing, and the energy based average energy release rates calculated for the static DCB testing.

Table 5.2. Average initiation energy release rates for static and dynamic testing

Mode I / II Energy Release Rates			
Adherend		**Peak/Initiation J/m^2**	**Average J/m^2**
6.4 mm Al DCB	Static	1800	610
	Dynamic	1900	N/A
36 ply Composite DCB	Static	1200	440
12 ply Composite DCB	Static	2700	510
	Dynamic	1400	N/A
12 ply Composite ELS	Dynamic	3100	N/A
12 ply Composite SLB	Mode I	1000	N/A
	Mode II	1400	N/A

As previously mentioned, the 12 ply static DCB results were significantly higher than the aluminum and 36 ply composite static DCB results due to the reduced local loading rate resulting from the lower stiffness of the 12 ply adherends. This loading rate effect was also seen in the difference between the 12 ply static and dynamic results, as the lower quasi-static test rate allowed for a larger plastic zone and thus a higher initiation energy release rate. Mode II critical energy release rates were also found to be higher than mode I, as is commonly reported in the literature.

The test results were also used to construct a preliminary failure envelope, which is shown in Figure 5.24. The data points represent the average critical energy release rates obtained for the mode II and mixed-mode dynamic testing and the peak values previously presented for the dynamic DCB testing. A rough failure curve was drawn through the data points to illustrate the region where the final loci of failure may be located. When fully developed through further testing, the failure envelope encompassed by the loci could be used for the chosen adhesive/composite system in the same manner that the current failure criteria for design with metals are being used for design purposes.

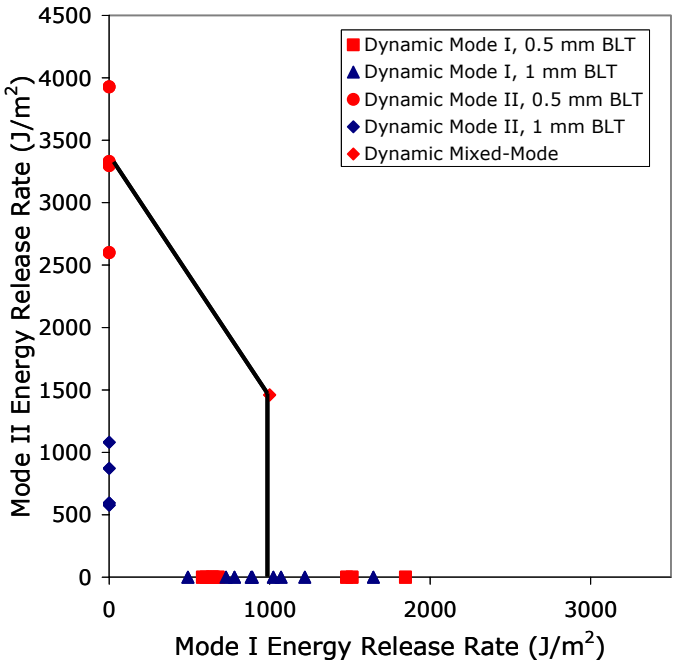

Figure 5.24. Mode I/II Fracture Failure Envelope

References

1. Blackman, B.R.K., Dear, J.P., Kinloch, A.J., Macgillivray, H., Wang, Y., Williams, J.G., Yayla, P., "The failure of fibre composites and adhesively bonded fibre composites under high rates of test. Part I: Mode I loading-experimental studies," *Journal of Materials Science*, **30** (1995), 5885-5900.
2. Lai, Y.-H., Dillard, D.A., "Using the fracture efficiency to compare adhesion tests," *International Journal of Solids Structures,* **4** (1997), 509-525.
3. Gagliano, J.M., "An Improved Method for the Fracture Cleavage Testing of Adhesively-Bonded Wood." Thesis, Virginia Tech, 2001.
4. Yamini, S., Young, R.J., "The mechanical properties of epoxy resins part II: Effect of plastic deformation upon crack propagation," *Journal of Materials Science*, **15** (1980), 1823-1831.

Chapter 6: Summary and Recommendations

6.1: Accomplishments and Observations

The test and analysis methods presented in this thesis provide the tools to collect data necessary for design with the chosen adhesive/composite system. A significant amount of mode I, II, and mixed-mode I/II fracture data was collected and test and analysis methods were refined to improve repeatability as well as ease of use. Static and dynamic DCB data was collected on aluminum and composite adherends and dynamic ELS and SLB data was collected using 12 ply composite adherends. Unstable crack growth was found in both static and dynamic mode I testing and crack growth immediately jumped to the composite adherends upon initiating from the cohesive precrack in mode II and mixed-mode dynamic testing.

Through refinement, specimen preparation methods were improved considerably, reducing the amount of error in test data due to inconsistencies in test specimens. The use of a platen press for composite specimens significantly reduced the bondline thickness variation, especially for the thinner 11 and 12 ply composites. The final curing procedure allows for complete adhesive curing, eliminating issues resulting from differing cures between specimen batches. Unlike preliminary testing, no noticeable batch to batch variation was found in fully cured specimens prepared in the press.

Along with the data collected for use in design, the methods developed to collect and analyze dynamic fracture data may lead the way for future work in this field. These image based data collection methods provide an alternate means for gathering data in situations where the use of load cells and sensors may not be feasible due to loading rate, loading method, or test environment. The work of this thesis provides the tools to collect dynamic mode I, II, and mixed-mode data using a high speed imaging system for the

DCB, ELS, and SLB geometries, and can be easily adapted to other geometries, including asymmetric versions of the aforementioned tests. Future work will include the development of a method to visually obtain dynamic mode III data as well.

An average energy release rate based on an energy balance was also developed to possibly provide a design parameter that falls between the high initiation values and the low arrest values found as a result of unstable crack growth. This method provides a feasible means to obtain usable results from test cases where unstable crack growth dominates. This energy balance based average energy release rate can be applied to static and dynamic test results, but was only used statically in this thesis due to an insufficient sampling rate for dynamic testing.

6.2: Successes and Areas for Improvement

As previously mentioned, the edge detection method for visually measuring specimen displacements was successfully adapted to the chosen system in all of the loading modes presented in this thesis. This method had been previously used on a different type of adhesive/adherend system with excellent results, and after modification, was shown to work well in this case upon verification with hand calculations. Through refinement, this method was also improved to provide more consistent results with less noise.

The developed ELS and SLB analysis methods were also shown to be effective through sensitivity analyses as well as hand calculations. The least-squares method developed to determine crack length for these geometries is the first known of its kind and through much development and refinement, was found to be very effective for the

chosen test rate. The methods employed for these geometries may open doors for further dynamic testing in modes I-III for other systems.

Although significant improvement was made throughout the duration of this work, there are a few things that need addressing. The issue of nonlinearity in regard to the dynamic ELS testing needs to be further investigated, through numerical analysis or possibly by applying large deflection beam theory to test results. Also, the loading rate effects for dynamic testing may need to be investigated to determine whether there are dynamic effects influencing the test data. With the use of a higher speed camera capable of capturing discrete initiation and arrest points for dynamic tests, the energy based average method described in this thesis could provide some insight into these effects. A numerical investigation of these dynamic effects would also be an invaluable supplement to the experimental results.

6.3: Future Work

Although much work was completed, more testing is still necessary to fully define the failure characteristics of the chosen system in modes I and II. Because of time constraints, only one dynamic mixed-mode I/II test was conducted. Also, bonding issues were discovered with 1 mm bondline thickness dynamic mode II specimens, leading to siginificant doubt in the results obtained for these tests. As a result of these issues, more SLB tests with both a 1 mm and 0.5 mm bondline thickness as well as more ELS tests with a 1 mm bondline thickness will be necessary to fully characterize the adhesive under dynamic mode I-II loading. Asymmetric tests using the DCB, ELS, and SLB geometries would also be helpful in more fully characterizing the mixed-mode region of the failure envelope.

With the use of an imaging system with a higher sampling rate, it would also be possible to calculate energy-based averages for dynamic tests, allowing for comparisons to be made with the static averages. A higher sampling rate would also allow for better characterization of the initiation and arrest events during the dynamic tests, possibly leading to further insights into the dynamic behavior of the chosen system.

Another issue that needs to be investigated is possible non-linearity in dynamic ELS tests. Large deflections are necessary for crack propagation, thus causing displacements that may exceed the limitations of linear beam theory. As previously mentioned, this issue could be investigated through numerical analysis of this geometry at large deflections, as well as applying large displacement beam theory to define any discrepancies between these results and those calculated using linear beam theory.

Numerical analysis on the effects of different beam stiffnesses would also be helpful. As previously mentioned, the less stiff 12 ply adherends produced higher initiation energy release rates than those collected with 36 ply and aluminum adherends due to slower loading. A numerical analysis using varying adherend stiffnesses could possibly provide more explanation on this phenomenon as well as provide more backing for experimental results. Also, a numerical investigation of the effects of crack lengths longer than 100 mm would provide helpful backing for the experimental results which showed higher energy release rates at longer crack lengths.

Numerical analyses of other aspects of this work would also be very helpful in determining some of the behavior seen in both static and dynamic testing. Dynamic analyses could provide insight into the effects of a high loading rate on test results such as wave propagation and could also help explain the viscoelastic effects of the adhesive in both static and dynamic testing. A better collaboration between the numerical and

experimental groups involved in this work could provide substantially more progress as well as insight into the many intricacies of the chosen adhesive/composite system.

Appendix A: Hutchinson and Suo Analysis

Hutchinson and Suo developed a general solution for the fracture of an infinite layer with a crack[1]. This geometry is shown in Figure A.1 and assumes an isotropic, homogeneous and linear elastic material that is loaded along three edges.

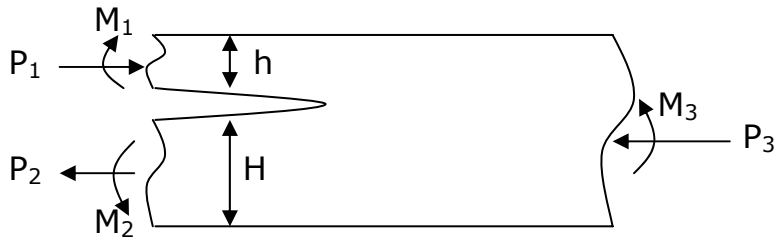

Figure A.1. Moments and forces for Hutchinson and Suo analysis

This analysis utilizes three end loads and three moments, as well as two beam thicknesses to vary the mode mixity at the crack tip. The beam thicknesses are the fundamental elements of the analysis, defining nine geometric parameters:

$$\eta = \frac{h}{H}, \tag{1}$$

$$C_1 = \frac{1}{1/\eta + 1}, \tag{2}$$

$$C_2 = \frac{6/\eta}{(1/\eta + 1)^3}, \tag{3}$$

$$C_2 = \frac{1}{(1/\eta + 1)^3}, \tag{4}$$

$$\frac{1}{U} = 1 + 4\eta + 6\eta^2 + 3\eta^3, \tag{5}$$

$$\frac{1}{V} = 12\left(1 + \eta^3\right), \tag{6}$$

$$\frac{\sin\gamma}{\sqrt{UV}} = 6\eta^2\left(1 + \eta\right), \tag{7}$$

$$\omega = 52.1^0 - 3^0 \eta \tag{8}$$

where ω (different than that found in the mixed-mode failure criteria) varies slowly with η[1]. Linear combinations of the applied loads are then combined to form the generalized loading parameters:

$$P = P_1 - C_1 P_3 - \frac{C_2 M_3}{h}, \tag{9}$$

$$M = M_1 - C_3 M_3 \tag{10}$$

where C_1, C_2, and C_3 are defined by equations 2, 3, and 4. Finally, the geometric parameters and generalize loading parameters are combined to determine the mode I and mode II stress intensity factors:

$$K_I = \frac{P}{\sqrt{2hU}} \cos\omega + \frac{M}{\sqrt{2h^3 V}} \sin(\omega + \gamma), \tag{11}$$

$$K_{II} = \frac{P}{\sqrt{2hU}} \sin\omega - \frac{M}{\sqrt{2h^3 V}} \cos(\omega + \gamma) \tag{12}$$

For the purpose of this thesis, these stress intensity factors were equated to energy release rates using the equation:

$$G = \frac{K^2}{E} \tag{13}$$

where E is the modulus of elasticity of the material. This equation assumes a plane stress condition so it is an approximation, but it is useful in showing the range that the phase angles will fall into for the chosen geometries. The values for energy release rate were then plotted as a function of the applied load for the available adherend thicknesses (2.5, 2.8, 6.5, and 8.5 mm) to determine the possible mode mixities with the supplied materials. The geometries used for this analysis were the double-cantilever beam, symmetric for mode I and asymmetric for mixed-mode fracture, the single leg bend for

mixed-mode fracture (both symmetric and asymmetric), and the end-loaded split for mode II (symmetric) and mixed mode (asymmetric) fracture. Asymmetric geometries were created using a 2.5 mm and an 8.5 mm adherend. The resulting mode-mixity plot is shown in Figure A.2.

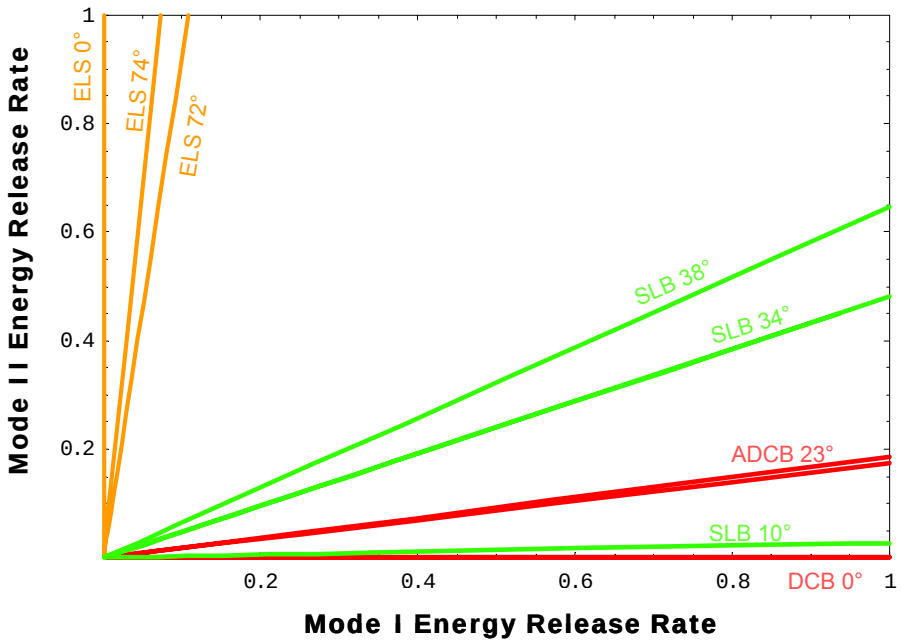

Figure A.2. Possible mode mixities determined with Hutchinson and Suo method

References

1. Hutchinson, J.W., Suo, Z., "Mixed Mode Cracking in Layered Materials," *Advance in Applied Mechanics*, **29** (1992), 63-189.

Appendix B: Crack Tip Blunting Model

Kinloch and Williams present a model for the blunting of a crack tip in an adhesive layer[1]. As previously mentioned, the yield stresses influence the degree of plastic deformation at the crack tip, and as a result the measured toughness and type of crack growth (stable or unstable). The authors developed this model based on the stress distributions at the crack tip, and determined that the stress normal to the crack tip at a distance r ahead of the tip is defined as:

$$\sigma_{yy} = \frac{\sigma_0 \sqrt{a}}{\sqrt{2r}} \frac{1 + \frac{\rho}{r}}{\left(1 + \frac{\rho}{2r}\right)^{3/2}} \qquad (1)$$

where σ_0 is the applied stress, ρ is the crack tip radius, and a is the crack length. If this stress is large, the crack propagates stably, whereas if this value decreases due to changes in the test conditions or adhesive makeup, the crack propagates in an unstable manner[2]. If it is assumed that fracture occurs at a distance of r=c at a critical stress σ_c, then Equation 1 can be expressed as:

$$\frac{\sigma\sqrt{\pi a}}{\sigma_c \sqrt{2\pi c}} = \frac{\left(1 + \frac{\rho}{2c}\right)^{3/2}}{1 + \frac{\rho}{c}} \qquad (2)$$

and the term $\sigma_c \sqrt{2\pi c}$ is equivalent to K_{IC}, the critical stress intensity factor for a sharp crack, and $\sigma\sqrt{\pi a}$ is equivalent to K_{IB}, the critical stress intensity factor for a blunt crack[1]. Thus:

$$\frac{K_{IB}}{K_{IC}} = \frac{\left(1 + \frac{\rho}{2c}\right)^{3/2}}{1 + \frac{\rho}{c}} \qquad (3)$$

where $K_{IB}/K_{IC} > 1$ indicates unstable propagation, and $K_{IB}/K_{IC} < 1$ indicates stable propagation[1]. Kinloch and Williams found the highest value of K_{IB}/K_{IC} to be 2.0 for a DGEBA/3° amine that exhibited the largest crack jumps of all of the systems they tested. For the case of the adhesive tested for this thesis, the value of K_{IB}/K_{IC} is approximately 1.8, indicating unstable propagation according to the crack blunting model, which aligns with what was found experimentally.

References

1. Kinloch, A.J., Williams, J.G., "Crack blunting mechanisms in polymers," *Journal of Materials Science*, **15** (1980), 987-996.
2. Yamini, S., Young, R.J., "The mechanical properties of epoxy resins part II: Effect of plastic deformation upon crack propagation," *Journal of Materials Science*, **15** (1980), 1823-1831.

Appendix C: P2 Etching Process

1. Chemical solutions used:

    a. 5% NaOH Solution (Weight/Weight)
        For 4L of Solution:
        i. 200g NaOH
        ii. 3800g Deionized Water

    b. 50% HNO_3 Solution (Volume/Volume)
        For 4L of Solution:
        i. 2L of Nitric Acid
        ii. 2L Deionized Water

    c. P2 Solution Fe(III)
        For 4L of Solution:
        i. 505.2g $Fe_2(SO_4)_3 \cdot 4H_2O$
        ii. 740g H_2SO_4 concentrate
        iii. Add deionized H_2O until you have 4L of solution

2. Abrade adherend surface w/ Scotch Brite™ Pad and clean with Acetone
3. Rinse with deionized (DI) water
4. Put in NaOH solution at 50°C for 2-3 minutes
5. Rinse with DI water
6. Put in HNO_3 solution at room temp for 2-3 minutes
7. Rinse with DI water
8. Put in P2 solution at 60°C for 8 minutes
9. Rinse with DI water
10. Heat off DI water in oven at 100°C for 12 hours

Appendix D: Mode II/Mixed-Mode Analysis Code

ELS Crack Length Determination Code Example-Ideal Data Set Case

■ **Specimen Length and Opening Displacement**

In[1]:=
```
L = 200; Δ = 1.0;
```

■ **Theoretical Equation Definition**

In[2]:=
```
v[x_, a_] := (If[x ≤ a,
                vv = -((6 a^3 + 2 L^3 - 9 a^2 x - 3 L^2 x + 4 x^3) Δ) / (2 (3 a^3 + L^3)),
                vv = -((L - x)^2 (2 L + x) Δ) / (2 (3 a^3 + L^3))];
              vv)
```

In[3]:=
```
dv[x_, a_] := (If[x ≤ a,
                dvv = -((9 a x (3 a^3 + 3 a L^2 - 2 L^3 - 4 a x^2) Δ) / (2 (3 a^3 + L^3)^2)),
                dvv = (9 a^2 (L - x)^2 (2 L + x) Δ) / (2 (3 a^3 + L^3)^2)];
              dvv)
```

■ **Importation of Test Data (Ideal Case Created for this Example)**

In[4]:=
```
exp = {};
Do[x1 = i * L / 30; v1 = v[x1, 125]; AppendTo[exp, {x1, v1}], {i, 0, 30}]
TableForm[exp] // N
```

Out[6]//TableForm=

0.	-1.
6.66667	-0.93736
13.3333	-0.874976
20.	-0.813105
26.6667	-0.752004
33.3333	-0.691929
40.	-0.633136
46.6667	-0.575883
53.3333	-0.520426
60.	-0.467021
66.6667	-0.415926
73.3333	-0.367395
80.	-0.321687
86.6667	-0.279057
93.3333	-0.239762
100.	-0.204059
106.667	-0.172204
113.333	-0.144453
120.	-0.121064
126.667	-0.10218
133.333	-0.0855151
140.	-0.070133
146.667	-0.0560979
153.333	-0.0434737
160.	-0.0323247
166.667	-0.0227149
173.333	-0.0147086
180.	-0.00836979
186.667	-0.00376266
193.333	-0.000951355
200.	0.

■ **Least Squares Fit of Experimental Data from Theoretical Equations**

In[7]:=
```
nmax = Length[exp]
```

Out[7]= 31

In[8]:=
```
f[a_] := Sum[(v[exp[[n, 1]], a] - exp[[n, 2]])^2, {n, 1, nmax}]
```

In[9]:=
```
f[0]
```

Out[9]= 0.151226

In[10]:=
```
f[100]
```

Out[10]= 0.00578132

In[11]:=
```
f[203]
```

Out[11]= 0.17024

In[12]:=
```
p1 = Plot[f[a], {a, 0, L}]
```

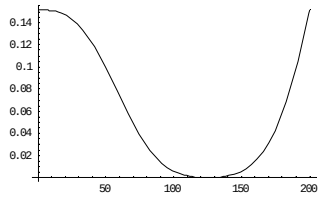

Out[12]= - Graphics -

In[13]:=
```
df[a_] := Sum[2 (v[exp[[n, 1]], a] - exp[[n, 2]]) * dv[exp[[n, 1]], a], {n, 1, nmax}]
```

In[14]:=
```
p2 = Plot[df[a], {a, 0, L}]
```

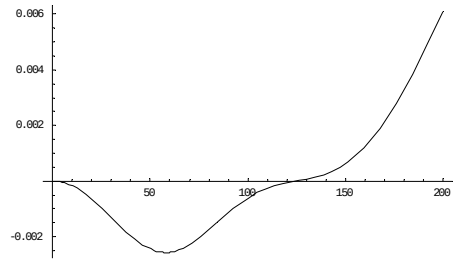

Out[14]= - Graphics -

In[15]:=
```
Show[GraphicsArray[{{p1}, {p2}}]]
```

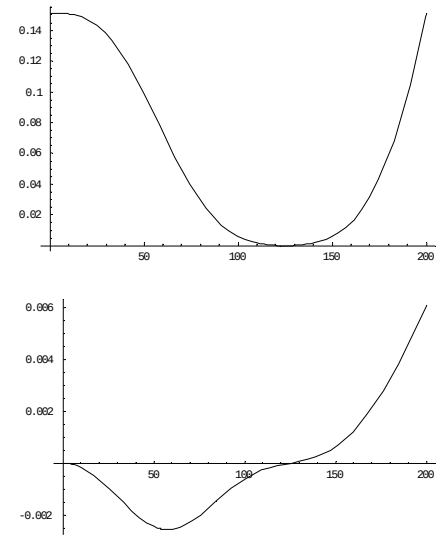

Out[15]= - GraphicsArray -

■ **Crack Length Determination**

In[16]:=
```
FindRoot[df[a] == 0, {a, 120, 130}]
```

Out[16]= {a → 125.}

■ SLB Crack Length Determination Code Example- Ideal Data Set Case

Determination of the crack length "a" from discrete lateral deflection data via least squares fit to the lateral deflection of beam theory.

▪ Geometric Parameters

In[49]:=
```
L = 200; Δ = 1.0; d = 10;
```

Note: Dimensions in mm. Arm 2 displaces as a rigid body and does not contribute to the strain energy. Only portions 1 and 3 deform. Length c = d + a, where nominally d = 10 mm, and "a" is the crack length.

▪ Theoretical Equation Definition

In[50]:=
```
v[x_, c_] := (If[x ≤ c,
                 vv = -((14 c^3 + 2 L^3 - 21 c^2 x - 3 L^2 x + 8 x^3) Δ)/(2 (7 c^3 + L^3)),
                 vv = -((L - x)^2 (2 L + x) Δ)/(2 (7 c^3 + L^3))];
              vv)
```

In[51]:=
```
dv[x_, c_] := (If[x ≤ c,
                  dvv = -((21 c x (7 c^3 + 3 c L^2 - 2 L^3 - 8 c x^2) Δ)/(2 (7 c^3 + L^3)^2)),
                  dvv = (21 c^2 (L - x)^2 (2 L + x) Δ)/(2 (7 c^3 + L^3)^2)];
               dvv)
```

▪ Importation of Test Data (Ideal Case Created for this Example)

In[52]:=
```
exp = {};
Do[x1 = i * L / 30; v1 = v[x1, 75]; AppendTo[exp, {x1, v1}], {i, 0, 30}]
TableForm[exp] // N
```

Out[54]//TableForm=

0.	-1.
6.66667	-0.92764
13.3333	-0.85593
20.	-0.785518
26.6667	-0.717054
33.3333	-0.651186
40.	-0.588565
46.6667	-0.529839
53.3333	-0.475658
60.	-0.42667
66.6667	-0.383526
73.3333	-0.346874
80.	-0.315526
86.6667	-0.285351
93.3333	-0.25623
100.	-0.228245
106.667	-0.201478
113.333	-0.176009
120.	-0.15192
126.667	-0.129292
133.333	-0.108205
140.	-0.0887418
146.667	-0.0709826
153.333	-0.0550088
160.	-0.0409016
166.667	-0.028742
173.333	-0.0186113
180.	-0.0105906
186.667	-0.00476103
193.333	-0.00120378
200.	0.

▪ Least Squares Fit of Experimental Data from Theoretical Equations

In[55]:=
```
nmax = Length[exp]
```

Out[55]= 31

In[56]:=
```
f[a_] := Sum[(v[exp[[n, 1]], d + a] - exp[[n, 2]])^2, {n, 1, nmax}]
```

In[57]:=
```
f[0]
```

Out[57]= 0.182925

In[58]:=
```
f[65]
```

Out[58]= 0.

In[59]:=
```
f[180]
```

Out[59]= 0.124377

In[60]:= **p1 = Plot[f[a], {a, 0, L}]**

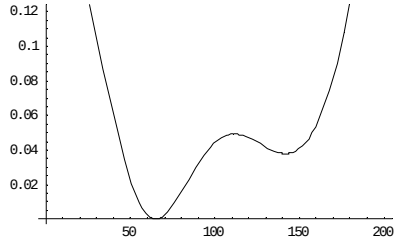

Out[60]= **- Graphics -**

In[61]:= **df[a_] := $\sum_{n=1}^{nmax}$ 2 (v[exp[[n, 1]], d + a] - exp[[n, 2]]) * dv[exp[[n, 1]], d + a]**

In[62]:= **p2 = Plot[df[a], {a, 0, L}]**

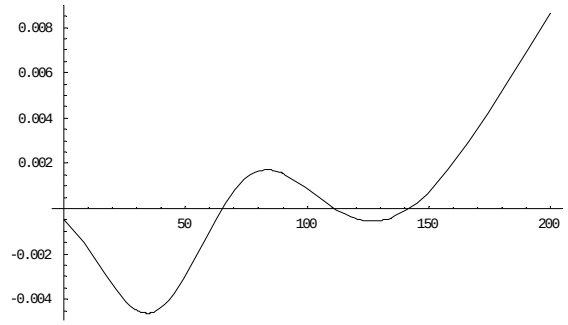

Out[62]= **- Graphics -**

In[63]:= **Show[GraphicsArray[{{p1}, {p2}}]]**

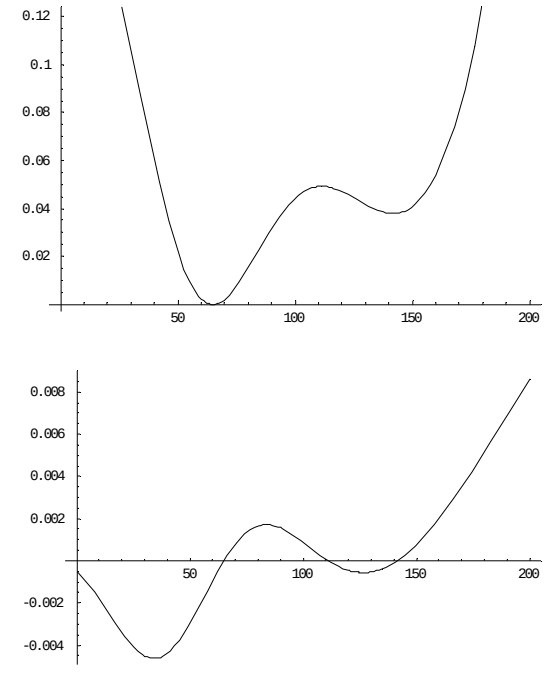

Out[63]= **- GraphicsArray -**

■ Crack Length Determination

In[64]:= **FindRoot[df[a] == 0, {a, 60, 70}]**

Out[64]= {a → 65.0002}